

The Spatio-Temporal Evolution of Solar Flares Observed with AIA/SDO: Fractal Diffusion, Sub-Diffusion, or Logistic Growth ?

Markus J. Aschwanden²

*Lockheed Martin Advanced Technology Center, Solar & Astrophysics Laboratory, Org. ADBS, Bldg.252,
3251 Hanover St., Palo Alto, CA 94304, USA; e-mail: aschwanden@lmsal.com*

ABSTRACT

We explore the spatio-temporal evolution of solar flares by fitting a radial expansion model $r(t)$ that consists of an exponentially growing acceleration phase, followed by a deceleration phase that is parameterized by the generalized diffusion function $r(t) \propto \kappa(t - t_1)^{\beta/2}$, which includes the logistic growth limit ($\beta = 0$), sub-diffusion ($\beta = 0 - 1$), classical diffusion ($\beta = 1$), super-diffusion ($\beta = 1 - 2$), and the linear expansion limit ($\beta = 2$). We analyze all M and X-class flares observed with GOES and AIA/SDO during the first two years of the SDO mission, amounting to 155 events. We find that most flares operate in the sub-diffusive regime ($\beta = 0.53 \pm 0.27$), which we interpret in terms of anisotropic chain reactions of intermittent magnetic reconnection episodes in a low plasma- β corona. We find a mean propagation speed of $v = 15 \pm 12 \text{ km s}^{-1}$, with maximum speeds of $v_{max} = 80 \pm 85 \text{ km s}^{-1}$ per flare, which is substantially slower than the sonic speeds expected for thermal diffusion of flare plasmas. The diffusive characteristics established here (for the first time for solar flares) is consistent with the fractal-diffusive self-organized criticality (FD-SOC) model, which predicted diffusive transport merely based on cellular automaton simulations.

Subject headings: Sun: Solar Flares — Statistics — magnetic fields

1. INTRODUCTION

Many physical processes can be characterized by their spatio-temporal evolution, which we simply define here as the temporal evolution or time dependence of a spatial or geometric parameter, say $x(t)$, where the geometric parameter x could be a spatial length scale, an area, a volume, a fractal dimension, or any combination of these. At the largest scales, for instance, the Big Bang theory describes the evolution of the universe by the gradual expansion of its radius $r(t)$, which can be decelerating in a closed universe (Friedmann-Lemaître-Robertson-Walker model). Recent supernova observations reveal an accelerating universe at $z \approx 0.5$ (Riess et al. 1998; Perlmutter et al. 1999), and a deceleration that preceded the current epoch of cosmic acceleration (Riess et al. 2004).

Other dynamic processes that predict a specific spatio-temporal evolution based on some physical model include Brownian motion, fractal Brownian motion, classical diffusion, sub-diffusion, super-diffusion, Lévy flights, logistic growth, percolation, self-organized criticality avalanches, cellular automata, non-extensive Tsallis entropy, complex networks, etc. The knowledge of the spatio-temporal evolution of a physical process is often directly related to scaling laws between various physical parameters, and thus spatio-temporal measurements play a decisive role in the derivation of scaling laws. For instance, particle conservation ($nV = \text{const}$) in an expanding gas, plasma, or universe predicts a reciprocal scaling between the particle density $n(t)$ and the volume $V(t)$, i.e., $n(t) \propto V(t)^{-1}$, and consequently a scaling of $n(t) \propto r(t)^{-3}$ as a function of the radius $r(t)$ in the case of homogeneous isotropic expansion, while it scales as $n(t) \propto r(t)^{-D}$

for a fractal volume with Hausdorff dimension $D < 3$. The existence of a spatio-temporal evolution, such as $n(t) \propto r(t)^{-3}$ for adiabatic expansion, implies then also the prediction of a statistical correlation or scaling law $n \propto r^{-3}$, if the expansion speeds $v = \partial r / \partial t$ of the sample have a limited range.

Needless to say, that scaling laws obtained from solar data, where we have ample spatial resolution, are extremely useful for the interpretation of stellar data, where we have no spatial resolution at all and have to rely on scaling laws measured in solar or magnetospheric plasmas. Here we focus on the spatio-temporal evolution of solar flares, which is a completely unexplored topic, but bears important information on the underlying dynamic processes. There are very few statistical measurements of spatial scales L , areas A , and volumes V , or fractal dimensions D of solar flares, and virtually no statistical studies about the temporal evolution of these parameters, such as $L(t), A(t), V(t), D(t)$. A few statistical measurements of spatio-temporal parameters of solar flares (compiled in Aschwanden 1999) have been made from the S-054 soft X-ray imager onboard *SkyLab* (Pallavicini et al. 1977), from *Yohkoh* soft X-ray images (Kano and Tsuneta 1995; Porter and Klimchuk 1995; Aschwanden et al. 1996; Metcalf and Fisher 1996; Reale et al. 1997; Shimizu 1997; Garcia 1998; Nagashima and Yokoyama 2006), from the *Multispectral Solar Telescope Array (MTSA)* rocket flight (Kankelborg et al. 1997), from the extreme-ultraviolet (EUV) imager SOHO/EIT (Berghmans et al. 1998; Krucker and Benz 2000), and from the EUV imager on TRACE (Aschwanden et al. 2000; Aschwanden and Parnell 2002; Aschwanden and Aschwanden 2008a,b). Most of these studies provide statistics on spatial length scales L , areas A , and durations T of flares (down to nanoflares), but there exists no study to our knowledge that provides statistics on the spatio-temporal evolution $L(t)$ or $A(t)$ of solar flares.

In this paper we are going to analyze the spatio-temporal evolution of all large (GOES X- and M-class) flares observed during the first two years of the SDO mission, which were observed with high spatial resolution ($0.6''$), high cadence (12 s), and in 7 coronal wavelengths filters that cover a wide temperature range ($T \approx 0.5 - 16$ MK). This is an ideal data set for such a study, because both spatial and temporal parameters can be measured with unprecedented accuracy and 100% time coverage. Setting a threshold of $>M1.0$ GOES class, we obtain a complete set of 155 flare events detected with both GOES and AIA, which makes it to a perfect representative statistical sample. The data analysis presented here is restricted to the 335 Å filter, which appears to be very suitable to capture the high-temperature component of the energy release and heating phase of these largest flares. We fit then various theoretical models to the measured time profiles of the flare areas $A(t)$ or mean radius $r(t) \propto A(t)^{1/2}$, such as: classical diffusion, $r(t) \propto t^{1/2}$; sub-diffusion $r(t) \propto t^{\beta/2}$ with $\beta < 1$; super-diffusion or Lévy flights, $r(t) \propto t^{\beta/2}$ with $\beta > 1$; or logistic growth, where the time profile initially expands exponentially and then saturates at a finite level, a limit that is also called *carrying capacity* of limited resources in ecological models. The generic form of these spatio-temporal evolution functions $r(t)$ are shown in Fig. 1. From the fits of the theoretical models to the observed flare data we aim then to gain physical insights into the underlying dynamic processes, which concern the spatial propagation (or chain reaction) of magnetic reconnection or other nonlinear energy dissipation processes. A particular statistical model that we test is the so-called *fractal-diffusion self-organized criticality model*, which predicts specific spatio-temporal evolutions and powerlaw distributions of the spatial and temporal parameters.

The plan of this paper consists of a brief description of relevant theoretical models (Section 2), the statistical data analysis and forward-fitting to 155 flare events observed with AIA/SDO (Section 3), a discussion of the interpretation and consequences of the results (Section 4), conclusions (Section 5), and a generalization of the FD-SOC model (Appendix A).

2. THEORETICAL MODELS

In the following we introduce some general theoretical models that describe the spatio-temporal evolution of physical systems, which have some universal validity for the dynamics of a large number of nonlinear and complex systems. The reason for their universal validity and applicability lies in the fact that they are formulated only in terms of the fundamental parameters of space and time, while individual applications generally involve more specific physical parameters (such as densities, temperatures, or magnetic fields in astrophysical applications).

2.1. Classical Diffusion and Brownian Motion

Classical diffusion obeys the following differential equation,

$$\frac{\partial f(x, t)}{\partial t} = \kappa \frac{\partial^2 f(x, t)}{\partial x^2}, \quad (1)$$

where $f(x, t)$ is the spatio-temporal distribution function of particles and κ is the diffusion coefficient. The diffusion equation, expressed here for a 1-dimensional (1-D) space coordinate x , can be generalized to 2-D or 3-D space, where x then signifies the distance r from the center position of the initial distribution. The solution of the diffusion equation is a Gaussian distribution function (Einstein 1905),

$$f(x, t) = \frac{1}{(4\pi\kappa t)^{1/2}} \exp(-x^2/4\kappa t), \quad (2)$$

with a time-dependent evolution of its second moment,

$$\langle x^2 \rangle = 2\kappa t, \quad (3)$$

which simply means that its radial size $r(t) = \sqrt{\langle x^2 \rangle}$ evolves proportionally to the square root of the time,

$$r(t) \propto t^{1/2}, \quad (4)$$

since the start of the process from an initial δ -function. This spatio-temporal relationship has originally been applied to the molecular motion in a fluid (Brown 1828), and thus is also called *Brownian motion*, named after the Scottish botanist Robert Brown. Experimentally it can be demonstrated by watching the vibrations of a dust particle suspended in a fluid under a microscope. While the random walk of a single particle is stochastic and unpredictable at every time step, the average distance of the motion of an ensemble of particles or the radial expansion of the ensemble is well-characterized by the square-root relationship of Eq. (4), and is also called classical diffusion, or more popularly “the random walk of a drunkard”. Numerous applications of classical diffusion can be found in nature, laboratory physics, and astrophysics, such as the expansion of released gases, aerosols in the atmosphere, dust clouds from volcanos, plasma diffusion in fusion reactors, thermal diffusion in solar flare plasmas, or insect ecology in biophysics. For a recent textbook on applications of Brownian motion see, e.g., Earnshaw and Riley (2011).

2.2. Anomalous Diffusion, Sub-Diffusion, Super-Diffusion, Lévy Flights

Deviations from classical diffusion processes, also called *anomalous diffusion*, are often defined in terms of a non-linear dependence on time, characterized with a power law index β deviating from unity,

$$r(t) \propto t^{\beta/2} \quad \begin{cases} \beta < 1 & \text{(sub-diffusion)} \\ \beta = 1 & \text{(classical diffusion)} \\ \beta > 1 & \text{(super-diffusion or Lévy flight)} \end{cases} \quad (5)$$

We show the generic time evolution of a sub-diffusion process with $\beta = 1/2$ and a super-diffusion process with $\beta = 3/2$ in Fig. 1. Anomalous diffusion implies more complex properties of the diffusive medium than a homogeneous structure, which may include an inhomogeneous fluid or fractal properties of the diffusive medium. Anomalous diffusion was found in biology, such as active cellular transport, protein diffusion within cells, or diffusion through porous media (percolation phenomena).

Related to super-diffusion processes are *Lévy flights*, named after the French mathematician Paul Pierre Lévy by Mandelbrot (1982), which are defined similarly to super-diffusion processes (with $\beta > 1$ in Eq. 5) and lead to heavy-tailed (powerlaw) distribution functions $f(x, t)$, in excess of the Gaussian distribution functions (Eq. 2) obtained for classical diffusion. A popular example for Lévy flights is the random walk of sharks or other ocean predators, which abandon Brownian motion by occasional large-range jumps, when they do not find sufficient food. Other applications of Lévy walks involve diffusion on fractal structures, tracer diffusion in living polymers, turbulent rotating flows, electromagnetically driven flows, subrecoil laser cooling, chaos in a Josephson junction (electronic chip), or even the geographic travel of bank notes. For an overview see, e.g., Zumofen et al. (1999).

2.3. Fractal-Diffusion in Self-Organized Criticality Systems

Inhomogeneous media can be structured in complex patterns. One of the simplest complex patterns are fractal structures (Mandelbrot 1982), which can be characterized by a single parameter, such as the fractal dimension D . For instance, a cubic volume V with length L that has a space-filling Euclidean volume $V = L^3$, can have a fractal substructure with a fractal volume $V = L^D$, with $D < 3$ being the (fractal) *Hausdorff dimension*.

Such fractal volumes were found to describe well the avalanches in nonlinear dissipative systems in the state of self-organized criticality (SOC), which led to the *statistical fractal-diffusive model of a slowly-driven self-organized criticality system* (Aschwanden 2012). The prototype of a SOC model is the cellular automaton model, which numerically simulates the spatio-temporal evolution of a SOC avalanche by thresholded next-neighbor interactions. The “spatial diffusion” of a SOC avalanche is defined by an iterative mathematical re-distribution rule between next neighbors in a grid (i, j, k) , such as,

$$\begin{aligned} z(i, j, k) &= z(i, j, k) + 1 && \text{initial input} \\ z(i, j, k) &= z(i, j, k) - 8 && \text{if } z(i, j, k) \geq 8, \\ z(i \pm 1, j \pm 1, k \pm 1) &= z(i \pm 1, j \pm 1, k \pm 1) + 1 \end{aligned} \quad (6)$$

where z denotes the number of energy quanta in each node that are re-distributed in the nonlinear energy dissipation process of a SOC avalanche (Bak et al. 1987). It was found that the instantaneous volume change $dV(t)/dt$ of a SOC avalanche can be approximated with a fractal scaling (Aschwanden 2012),

$$\frac{dV(t)}{dt} \propto x(t)^D, \quad (7)$$

and evolves in space according to the classical diffusion law (Eq. 4)

$$r(t) \propto t^{1/2} . \quad (8)$$

This scaling law has been inferred from the spatio-temporal evolution of a few cellular automaton avalanches (see Fig. 3 in Aschwanden 2012), which constitutes a strong prediction for any observation of SOC systems in nature. This prediction, however, has never been tested with observational data, such as for solar flares, which we set out to test in this study for the first time.

2.4. Logistic Growth Model

Instabilities represent a loss of equilibrium and show often a time evolution that consists of an initial exponential growth phase (which we might call the “acceleration phase”), followed by quenching and saturation of the instability in the decay phase (which we might call “deceleration phase”). The total dissipated energy in such an instability is often approximately proportional to the unstable volume. We can then describe the exponential growth phase with a proportionality of the change of volume $dV(t)/dt$ to the instantaneous volume $V(t)$,

$$\frac{dV(t)}{dt} = \Gamma V(t) = \frac{1}{\tau_G} V(t) , \quad (9)$$

where Γ is the growth rate, and $\tau_G = 1/\Gamma$ denotes the e-folding growth time, which has the simple solution of an exponential function,

$$V(t) = V_0 \exp\left(\frac{t}{\tau_G}\right) . \quad (10)$$

A more general approach to describe both the exponential growth phase together with the saturation phase is the *logistic equation*, which has been widely used in ecologic applications, but has universal validity for nonlinear systems with limited free energy. The logistic equation is defined by a simple first-order differential equation, discovered by Pierre François Verhulst in 1845 (see textbooks on nonlinear dynamics, e.g., May 1974; Beltrami 1987, p.61; Jackson 1989, p.75; Aschwanden 2011, p.94),

$$\frac{dV(t)}{dt} = \frac{V(t)}{\tau_G} \left[1 - \frac{V(t)}{V_\infty} \right] , \quad (11)$$

where V_∞ represents the asymptotic limit that is reached in the saturation phase. In ecologic applications, the asymptotic limit V_∞ is also called *carrying capacity*, such as the total amount of available energy or resources that can be sustained world-wide. From Eq. (11) we see that the logistic equation approaches the exponential growth equation (Eq. 9) for small times (when $V(t) \ll V_\infty$), and the limit $dV(t)/dt \approx 0$ and $V(t) \approx V_\infty$ for large times. The explicit solution of Eq. (11) is,

$$V(t) = \frac{V_\infty}{1 + \exp\left(-\frac{t-t_1}{\tau_G}\right)} , \quad (12)$$

while the time derivative dV/dt (representing the energy dissipation rate dE/dt if the energy is proportional to the volume),

$$\frac{dV(t)}{dt} = \frac{V_\infty}{\tau_G} \frac{\exp\left(-\frac{t-t_1}{\tau_G}\right)}{\left[1 + \exp\left(-\frac{t-t_1}{\tau_G}\right)\right]^2} . \quad (13)$$

If we approximate the unstable volume with a spherical geometry, the spatial length scale or radius $r(t)$ is related to the volume $V(t)$ as,

$$V(t) = \frac{4}{3} \pi r(t)^3 , \quad V_\infty = \frac{4}{3} \pi r_\infty^3 , \quad (14)$$

which predicts the following spatio-temporal evolution $r(t)$,

$$r(t) = \frac{3}{4\pi} V(t)^{1/3} = r_\infty \left[1 + \exp\left(-\frac{t-t_1}{\tau_G}\right) \right]^{-1/3}. \quad (15)$$

A graphical illustration of this logistic growth function is shown in Fig. 1, which appears to conform to a lower limit of sub-diffusion processes (for $\beta \mapsto 0$). The logistic growth model was applied to population growth, neural networks, tumor growth in medicine, autocatalytic reactions in chemistry, the statistical distribution of fermions in atomic physics, language change in social sciences, or diffusion of innovations in economics. In solar physics, the logistic-growth model was applied to model hard X-ray pulses (Aschwanden et al. 1998) and magnetic energy storage in active regions (Wang et al. 2009).

2.5. Combining Logistic Growth and Diffusion Models

In order to have compatible models for the exponential growth phase, we adopt the same exponential growth phase of the logistic model (Eq. 15) for the diffusion models, so that the spatio-temporal evolution $r(t)$ differs only in the deceleration phase for the various models shown in Fig. 1. We choose the transition time between the acceleration and deceleration phase at $t = t_1$ in the formulation of the logistic growth curve (Eq. 15), which has the value r_1 and time derivative v_1 ,

$$r_1 = r(t = t_1) = 2^{-1/3} r_\infty, \quad (16)$$

$$v_1 = \frac{dr}{dt}(t = t_1) = \frac{2^{-4/3} r_\infty}{3 \tau_G} = \frac{r_1}{6\tau_G}. \quad (17)$$

Defining the diffusion radius $r(t)$ in the deceleration phase with a diffusion constant κ ,

$$r(t) = \kappa (t - t_k)^{\beta/2}, \quad (18)$$

which has the following value r_1 and time derivative v_1 at the transition time $t = t_1$,

$$r_1 = r(t = t_1) = \kappa (t_1 - t_k)^{\beta/2}, \quad (19)$$

$$v_1 = \frac{dr}{dt}(t = t_1) = \frac{\kappa\beta}{2} \left(\frac{r_1}{\kappa}\right)^{1-2/\beta}, \quad (20)$$

which have to match the boundary conditions r_1 and v_1 (Eqs. 16-17) of the exponential growth phase. From Eqs. (16)-(20) we obtain the constants t_1, r_∞, τ_G ,

$$t_1 = t_k + \left(\frac{r_1}{\kappa}\right)^{2/\beta}, \quad (21)$$

$$r_\infty = r_1 2^{1/3}, \quad (22)$$

$$\tau_G = \frac{r_1}{6 v_1}. \quad (23)$$

Thus the combined time profile $r(t)$ with a smooth transition from the exponential growth (acceleration) phase to the diffusion (deceleration) phase is,

$$r(t) = \begin{cases} r_\infty \left[1 + \exp\left(-\frac{t-t_1}{\tau_G}\right) \right]^{-1/3} & \text{for } t \leq t_1 \\ \kappa (t - t_k)^{\beta/2} & \text{for } t > t_1 \end{cases} \quad (24)$$

which has four free parameters for fitting, where we treat $(\kappa, t_k, \beta, r_1)$ as independent parameters, while (t_1, r_∞, τ_G) are constrained by the boundary conditions (Eqs. 21-23). For classical diffusion ($\beta = 1$) the number of free parameters reduces to three.

3. OBSERVATIONS AND DATA ANALYSIS

3.1. GOES and AIA Observations

We select all solar flare events detected with the *Geostationary Operational Environmental Satellites* (GOES) and the *Atmospheric Imaging Assembly* (AIA) on the *Solar Dynamics Observatory* (SDO) (Lemen et al. 2012) above a threshold of the M1.0 class level (which includes M- and X-class events) during the first two years of the SDO mission. The selected time era starts when the first science data from AIA became available, 13 May 2010, and ends on 31 March 2011 when we started the data analysis. The selected time period contains a total of 155 solar flare events larger than M1.0 class, including 12 events larger than X1.0 class. The flare time intervals, listed in Table 1, were taken from the official GOES flare catalog. We extracted AIA images in all 6 coronal wavelengths during the GOES flare time intervals, with AIA data being available in 100% of the cases, but restricted our analysis to the 335 Å filter (Fe XVI), which appears to be the most suitable filter to probe the high-temperature component of these largest flares, since the other filters that are sensitive to high temperatures (94 Å and 131 Å) have a double response to cooler plasma of $T \lesssim 1.0$ MK that is not yet well-calibrated (due to the incompleteness of the CHIANTI atomic data base for Fe lines at temperatures $\lesssim 10^6$ K). All AIA images have a cadence of $\Delta t = 12$ s and a pixel size of $\Delta x = 0.6'' \approx 435$ km, which corresponds to a spatial resolution of $2.5\Delta x = 1.5'' \approx 1100$ km. We normalized all AIA 335 Å images by the exposure time. The total number of analyzed images amounts to 11,767 AIA 335 Å images, which averages to 76 images per flare event and an average flare duration of 910 s.

3.2. Data Analysis Method

In order to quantify the spatio-temporal evolution of flares we measure the flare area above some threshold flux level, which was chosen in the AIA 335 Å filter at a constant level of $F_{thresh} = 100$ and 200 DN/s. This is well below the median flux value of $F_{med}(t = 0) = 518$ DN/s and mean of $\langle F(t = 0) \rangle = 687 \pm 645$ DN/s of the maximum flux values of the EUV images at the flare start time, defined by GOES. Thus the instantaneous flare area $a(t)$ at time t is defined by the number of pixels that have a flux F in excess of the threshold F_{thresh} ,

$$a(t_i) = N[F_{x,y}(t_i) \geq F_{thresh}] , \quad (25)$$

while the time-integrated flare area $A(t)$ is the combined area of all spatially overlapping instantaneous flare areas $a(< t)$,

$$A(t_i) = a(t = 0) \oplus a(t = 1) \oplus \dots \oplus a(t = t_i) , \quad (26)$$

where the symbol \oplus indicates a logical OR-function between the pixels contained in each instantaneous flare area before time t_i . Thus, the time-integrated flare area $A(t)$ is a monotonically increasing quantity that contains all flux pixels that exceeded the threshold F_{thresh} at any time before a given time t_i , i.e., during the flare time interval $0 \leq t \leq t_i$.

The spatial scale $r(t)$ of each (time-integrated) flare area $A(t)$ is then defined by the radius of an equivalent circular area,

$$r(t) = \sqrt{A(t)/\pi} . \quad (27)$$

The advantage to use the time-integrated flare area $A(t)$ over the instantaneous flare area $a(t)$ is the robustness against temperature effects such as conductive or radiative cooling, which can decrease the flux of flaring pixels below the flux threshold after some time. However, we tested our method for both options and found compatible results in the cases of flares with no rapid cooling.

3.3. Examples of Analyzed Flares

In Fig. 2 we show an example of the data analysis of a single event (#28), out of the 155 analyzed events. The GOES time profiles are shown on a linear flux scale (Fig. 2, top panel), with a start time of 2011 March 07, 19:43 UT, peak time 20:12 UT, end time 20:58 UT, and GOES class M3.7 ($= 3.7 \times 10^{-5} \text{ W m}^{-2}$), according to the official NOAA flare catalog. The flare duration is over an hour ($T = 4500 \text{ s}$).

At this point it might be appropriate to recall the definition of the flare duration used in the NOAA flare detection algorithm: The event starts when 4 consecutive 1-minute X-ray values have met all three of the following conditions: (i) All 4 values are above the B1 threshold; (ii) All 4 values are strictly increasing; (iii) The last value is greater than 1.4 times the value that occurred 3 minutes earlier. The peak time is when the flux value reaches the next local maximum. The event ends when the current flux reading returns to half of the peak value (<http://www.ngdc.noaa.gov/stp/solar/solarflares.html>).

We analyzed the same flare time interval from AIA 335 Å data, which amounts, with a cadence of $\Delta T = 12 \text{ s}$, to a total of $N_T = T/\Delta T = 4500/12 = 375$ images. The total solar flux $F_{sun}(t)$ during this time interval (Fig. 2, second panel) is shown along with the flux $F_{flare}(t)$ integrated over the flare area (approximately corresponding to the field-of-view shown in the bottom rows of Fig. 2). The agreement between the two flux profiles confirms the correct localization of the flare position, which is centered at the heliographic position N30/W48 for this event.

The flare area $A(t)$ is evaluated by counting the pixels above the threshold $F_{thresh} = 100 \text{ DN/s}$, (or 200 DN/s, respectively). The pixels of the time-integrated area combines all overlapping flare areas from earlier times $t > t_0$, since flare start. The radius $r(t) = \sqrt{A(t)/\pi}$ of the equivalent circular (monotonically growing) flare area $A(t)$ is shown in the third panel of Fig. 2 (histogrammed curve), fitted with the model $r(t)$ defined in Eq. (24) (shown with a solid curve in Fig. 2). The goodness-of-fit is simply evaluated from the average deviation normalized by the maximum flare radius, $r_{max} = \max[r(t)] = r(t_{end})$,

$$\Delta r/r_{max} = \frac{\langle r_{obs}(t) - r_{model}(t) \rangle}{r_{max}}, \quad (28)$$

which is $\Delta r/r_{max} = 1.3\%$ for the threshold of $F_{thresh} = 100 \text{ DN/s}$, or $\Delta r/r_{max} = 1.2\%$ for the threshold of $F_{thresh} = 200 \text{ DN/s}$, respectively. We determine the flare area for two different thresholds, in order to test the uncertainty and sensitivity of the best-fit model parameters on the threshold value. In this flare we obtain a diffusion coefficient of $\kappa = 117 \pm 10 \text{ pixel s}^{-1/2}$ and a diffusion index of $\beta = 0.47 \pm 0.08$, which demonstrates a relatively small uncertainty caused by the chosen two fixed flux thresholds (see values given in Fig. 2 and listed in Table 1).

Five snapshots of the time-integrated flare images are shown in the bottom panels of Fig. 2, rendered as preflare-subtracted flux (Fig. 2, fourth row), as well as highpass-filtered flux (Fig. 2, bottom row), showing the flare loop fine structure with enhanced contrast. The contours of the flare area $A(t)$ are also shown as black contour lines in the flare snapshot images. The flux $A(t = 0)$ is near zero at the beginning of the time series, indicating that the flare start time (defined by GOES) corresponds to an early phase when the 335 Å flux was near the chosen threshold.

The data analysis is also shown in condensed form for a selection of another 48 events (out of the 155 analyzed events) in Fig. 3, where we show the spatio-temporal evolution of the GOES 1-8 Å flux $f_{GOES}(t)$ (dotted curve), the EUV flux $f_{AIA}(t)$ of the 335 Å filter (dashed curve), and the spatial evolution of the radius $r(t)$ of the equivalent circular flare area (histograms in Fig. 3), along with the best fit of the diffusion model (Eq. 24) for the two flux thresholds of $F_{thresh} = 100$ and 200 DN/s (solid curves in Fig. 3), as well

as a (preflare-subtracted) time-integrated AIA 335 image at the end of the flare (right panels in Fig. 3). The examples show the enormous variety of morphological shapes of flare areas, which generally consist of groups or arcades of post flare loops (in different projections) with highly fractal substructures. We show also the contours of the final time-integrated flare area above a threshold of $F_{thresh} = 100$ DN/s in Fig. 3 (right panels), which generally encompasses a contiguous flare area. The time profiles reveal that the GOES flux generally peaks earlier than the EUV flux, although they start at similar times. The evolution of the flare radius $r(t)$ shows often a first expansion triggered by a precursor flare. In such cases, our fits apply to the main phase, while the area associated with the precursor is subtracted. Note the variety of β -values in different flares, ranging from the logistic limit $\beta \gtrsim 1$ to the classical diffusion limit of $\beta \approx 1$. The fits of the diffusion model $r(t)$ shown in Fig. 3 illustrate the adequacy of the functional form (Eq. 24) that fits the data always within a few percent accuracy, as well as the consistency of results obtained from different thresholds.

3.4. Statistical Results

The statistics of the observed parameters is visualized in form of histogram distribution functions shown in Fig. 4, as well as in form of correlations between pairs of parameters in Fig. 5. The best-fit parameters L , κ , β , and $q_{fit} = \Delta r/r_{max}$ are also listed in Table 1 for each flare, and the ranges, means, standard deviations, and medians are summarized in Table 2.

The length scale L , defined as the spatial radius of the flare area after subtraction of possible preflare areas, i.e., $L = \sqrt{r(t_{end})^2 - r(t_{start})^2}$, was found in a range of $L = 5 - 50$ Mm. The flare time scale T , which we define from the GOES flare start time to the peak time, e.g., $T = t_{peak} - t_{start}$, has a range of $T = 120 - 8460$ s (i.e., from 2 min to over 2 hours). The GOES flux ranges for this sample of M and X-class flares from $F_{GOES} = 10^{-5}$ to 6.9×10^{-4} W m $^{-2}$. The AIA 335 Å flux is found in the range of $F_{AIA} = 7 \times 10^4$ to 2.5×10^7 DN/s. Then we measured also the average expansion velocity $v = r_{max}/(t_{start} - t_{end}) = 3.3 - 103$ km s $^{-1}$, as well as the maximum velocity during the flare time interval, $v_{max} = 8 - 550$ km s $^{-1}$. These parameters ($L, T, F_{GOES}, F_{AIA}, v, v_{max}$) have approximate powerlaw distributions (Fig. 4, left and middle column).

The best-fit model parameters have nearly Gaussian distributions (Fig. 4, right column), which can be characterized by the mean and standard deviations: the diffusion coefficient $\kappa = 56 \pm 24$ km s $^{-\beta/2}$, the diffusion index $\beta = 0.53 \pm 0.27$, and the goodness-of-fit $\Delta r/r_m = 2.2 \pm 0.7\%$. Thus, the diffusion index, which is found in a range of $\beta = 0.04 - 1.35$, covers the entire range from logistic growth ($\beta \approx 0$), to sub-diffusion ($\beta \approx 1/2$), and classical diffusion ($\beta \approx 1$), but extends much rarer into the regime of super-diffusion or Lévy flights ($\beta \approx 3/2$). No case was found that approaches the limit of linear expansion ($\beta = 2$).

3.5. Parameter Correlations

Parameter correlations can reveal physical scaling laws. In Fig. 5 we show scatterplots between pairs of observed parameters ($L, V, T, F_{GOES}, F_{AIA}, v, v_{max}, \kappa, \beta$). Let us first discuss how these parameters depend on the fundamental length scale L of flares (Fig. 5). The flare duration T shows only a loose correlation with the length scale L , i.e., $T \propto L^{2.0 \pm 1.2}$ (panel a), or $L \propto T^{0.8 \pm 0.5}$ (panel d). Weak correlations are also found for the GOES flux $F_{GOES}(L)$ (panel b), the mean expansion velocity $v(L)$ (panel c), as a function of the length scale L . The strongest correlations are found between the AIA 335 Å flux and the length scale, i.e., $F_{AIA}(L) \propto L^{2.4 \pm 0.5}$ (panel e), or with the volume $F_{AIA}(V) \propto V^{0.8 \pm 0.2}$ (panel g), and the diffusion

coefficient $\kappa(L) \propto L^{0.9 \pm 0.1}$ (panel f). The former good correlation can be explained if the EUV emission is proportional to the total flare volume, in which case we expect $F_{AIA} \propto V \propto L^3$. The latter good correlation can be explained for sub-diffusion and logistic growth, where the diffusion equation $L \propto \kappa(t - t_1)^{\beta/2}$ shows only a weak dependence on the time duration due to the small value of the power index $\beta/2 \ll 1$, which yields almost a proportionality of $L \propto \kappa$.

Correlating all other parameter combinations we found five more cases that are worthwhile to mention, shown in the lower half of Fig. 5. The mean expansion velocity scales almost reciprocally with the flare duration, $v_{max}(T) \propto T^{-1.0 \pm 0.6}$ (panel h), which is consistent with a maximum speed that is independent of the length scale, so that the mean length scale $\langle L \rangle$ is a constant (with uncorrelated scatter) and yields $v_{max} = \langle L \rangle / T \propto T^{-1}$. The maximum velocity shows also a good correlation with the mean velocity, i.e., $v_{max}(v) \propto v^{1.4 \pm 0.4}$ (panel k). There is also an expected trend of correlated EUV and soft X-ray fluxes, i.e., $F_{AIA} \propto F_{GOES}^{1.9 \pm 1.4}$ (panel i). What is most interesting that comes out of this study, is that the diffusion coefficient is strongly correlated with the EUV flux, i.e., $\kappa \propto F_{AIA}^{0.4 \pm 0.1}$ (panel l), as well as with the soft X-ray flux, i.e., $\kappa \propto F_{GOES}^{0.6 \pm 0.3}$ (panel j).

4. DISCUSSION

In this study we measured spatial (L) and temporal scales (T) in solar flares and investigated for the first time their spatio-temporal evolution $L(t)$. We quantified the spatio-temporal evolution with a general diffusion equation that is quantified in terms of a diffusion coefficient κ and a diffusion powerlaw index β (Eq. 24). The theoretical range of the diffusion powerlaw index, $\beta = 0 - 2$ includes the limit of logistic growth ($\beta \approx 0$), sub-diffusion ($\beta \approx 1/2$), classical diffusion ($\beta = 1$), and super-diffusion or Lévy flights ($\beta = 3/2$). In the following we discuss the consequences of the results in the context of self-organized criticality models (section 4.1), diffusion processes in the photosphere (section 4.2), in the corona (section (4.3), and in solar flares (section 4.4).

4.1. Self-Organized Criticality Models

The size distribution of solar flare parameters (energy, peak count rates, durations) follow all powerlaw distribution functions that have been interpreted in terms of a slowly-driven nonlinear system in the state of self-organized criticality (SOC) (Lu and Hamilton 1993). A quantitative model that predicts the values of the powerlaw slopes and the associated correlations of physical parameters has been recently proposed, was tested with numerical simulations of cellular automaton models, and compared with solar flare statistics (Aschwanden 2012). The most fundamental parameters of SOC models are the spatial size (e.g., length scale L , area A , volume V) and the time duration T . In SOC models applied to astrophysical observations, generally a proportionality is assumed between the spatial volume V and the radiated fluence E , which can be justified by the linear relationship between the column depth $\int dz$ and emission measure $EM \propto \int n_e^2 dz$ for optically-thin EUV and soft X-ray emission. Consequently, the instantaneous fractal volume of a SOC avalanche (dV_S/dt) corresponds to the energy dissipation rate (dE/dt) or flux F , and the peak energy dissipation rate (dE/dt) $_{max}$ to the peak flux P .

While classical diffusion ($L \propto T^{1/2}$) was adopted in the *statistical fractal-diffusive avalanche model of a slowly-driven self-organized criticality system (FD-SOC)* (Aschwanden 2012), based on empirical evidence from cellular automaton models, we generalize the model for anomalous diffusion and for wavelength-

dependent flux-volume scaling law $F_\lambda \propto (dV_S/dt)^\gamma$ in Appendix A, which predicts slightly different correlation coefficients and powerlaw slopes of the distribution functions. In 3D-space ($S = 3$), for which a mean fractal dimension of $D_3 = 2.0$ is predicted, and using the measured range of the diffusion index $\beta \approx 0.1 - 1.0$ (Fig. 4) and $\gamma = 0.8$ (Fig. 5, panel g), the following powerlaw slopes are predicted by the generalized FD-SOC model (Appendix Eq. A14),

$$\begin{aligned}
 \alpha_L &= 3.0 \\
 \alpha_T &= 1 + (S - 1)\beta/2 \approx 1.1 - 2.0 \\
 \alpha_F &= 1 + (S - 1)/D_S\gamma = 2.25 \\
 \alpha_P &= 1 + (S - 1)/S\gamma = 1.83 \\
 \alpha_E &= 1 + (S - 1)/(D_S\gamma + 2/\beta) \approx 1.1 - 1.6
 \end{aligned}
 \tag{29}$$

For the size distributions of flare length scales L we expect in the framework of the FD-SOC model $\alpha_L = 3$, while our observations show $\alpha_L = 2.0$ (Fig. 4, first row, left panel). For the size distribution of flare durations T , classical diffusion predicts a slope of $\alpha_T = 2.0$ and sub-diffusion (with $\beta = 1/2$) predicts $\alpha_T = 1.5$, while our observations show $\alpha_T \approx 2.2$ (Fig. 4, second row, left panel). For the GOES flux F_G and AIA 335 flux F_A we measure powerlaw slopes of $\alpha_F = 1.92$ and $\alpha_F = 1.34$ (Fig. 4), while the FD-SOC model predicts $\alpha_F = 2.0$. In a much larger sample of over 300,000 GOES flares, a value of $\alpha_F = 1.98 \pm 0.11$ was found (Aschwanden and Freeland 2012), which is fully consistent with the FD-SOC model for classical diffusion ($\beta = 1$). Considering the small statistical sample of 155 flares analyzed here, the obtained powerlaw slope values seem to be not inconsistent with the FD-SOC model, given the relatively small range of less than a decade over which a powerlaw slope could be fitted.

Alternatively, we can compare the observed parameter correlations (Fig. 5) and compare with the predictions of the SD-SOC model (Appendix A). The most fundamental relationship for anomalous diffusion predicts $L \propto T^{\beta/2}$, which amounts to $L \propto T^{1/4}$ for sub-diffusion ($\beta = 1/2$), while our linear regression fit yields $L \propto T^{0.8 \pm 0.5}$ (Fig. 5, panel d), which has a large uncertainty due to the weak dependence and large scatter of L and T values. A tighter correlation is found between the EUV flux and the flare volume, i.e., $F_{AIA} \propto V^{0.8 \pm 0.2}$, which corroborates the standard assumption in SOC models that the observed flux or emission is approximately proportional to the emitting volume.

In summary, the small statistical sample of 155 flare events does not allow us to determine the statistical scaling laws (or correlations) between spatial L and temporal scales T or the powerlaw distributions $N(L)$ and $N(T)$ of spatial and temporal parameters with sufficient accuracy, and to test SOC models based on their statistical distributions. However, our study can quantify the spatio-temporal evolution $L(t)$ for individual flare events very accurately, which could potentially be compared with the spatio-temporal evolution $L(t)$ of cellular automaton simulations to test SOC models quantitatively. This could clarify whether SOC cellular automaton avalanches based on (thresholded) next-neighbor interactions can be statistically described by anomalous or classical diffusion processes. Diffusion-dominated dynamics (Bregman 2007, 2008) or diffusion entropy (Grigolini et al. 2002) has been applied to SOC avalanche models elsewhere.

4.2. Diffusion Processes in the Photosphere

Magnetic fluxtubes that emerge through the photosphere and build footpoints of coronal magnetic loops as well as postflare loops, are buffeted around by the random walk dynamics of subphotospheric magneto-convection. Measurements of the random motion of granules and supergranulation features have

been characterized with a diffusion equation,

$$\langle r^2 \rangle = 4Dt, \quad (30)$$

where the diffusion coefficient D is related to our definition $\sqrt{\langle r^2 \rangle} = \kappa t^{1/2}$ (Eq. 18) by $D = (\kappa/2)^2$. Thus, our measurements in solar flares with $\kappa = 56 \pm 24 \text{ km s}^{-1/2}$ would correspond to a range of $D \approx 300 - 1600 \text{ km}^2 \text{ s}^{-1}$. In comparison, photospheric random motion has been determined to $D = 110 \text{ km s}^{-1}$ in strong-field cores of active regions, and $D = 250 \text{ km s}^{-1}$ in the surrounding area (Schrijver and Martin 1990), $D = 200 - 400 \text{ km s}^{-1}$ from the motion of magnetic elements (Mosher 1977), $D = 120 - 230 \text{ km s}^{-1}$ from Quiet Sun magnetic patterns (Komm et al. 1995), which appears substantially lower than in flares. However, higher values have been inferred from the magnetic polarity reversal during a solar cycle ($D = 1100 \text{ km s}^{-1}$; Leighton 1964, 1969), from meridional flows ($D = 600 \text{ km s}^{-1}$; Wang et al. 1989; Zirin 1985), or from mottles ($D = 600 \text{ km s}^{-1}$ corrected for unresolved small-scale elements; Schrijver et al. 1996). In analogy to our fractal-diffusive SOC model (Aschwanden 2012), the dispersion of magnetic field elements across the solar surface was thought to be a diffusion process on a fractal geometry (Lawrence 1991). The diffusion of magnetic elements across the solar surface was actually found to have a 2-D fractal dimension of $D_2 = 1.56 \pm 0.08$ and an anomalous diffusion index of $\beta = 0.25 \pm 0.40$, similar to our result of preferential sub-diffusion ($\beta = 0.53 \pm 0.27$). In contrast, Ruzmaikin et al. (1996) found super-diffusion in photospheric random motion. A super-diffusive regime with $\beta \approx 1.48 - 1.67$ was also measured from the proper motion of bright points (Abramenko et al. 2011). Diffusion in the photosphere is also thought to be responsible for magnetic flux cancellation (Litvinenko 2011).

In summary, most diffusion processes observed in magnetic features in the photosphere are generally slower ($D \approx 100 - 600 \text{ km s}^{-1}$) than what we observe in flares ($D \approx 300 - 1600 \text{ km}^2 \text{ s}^{-1}$), and thus are unlikely to explain the observed spatial diffusion during flares.

4.3. Diffusion Processes in the Corona

The magnetic field evolution in the solar corona is usually described by the induction equation in the framework of ideal magnetohydrodynamics (MHD),

$$\frac{d\mathbf{B}}{dt} = \nabla \times (\mathbf{v} \times \mathbf{B}) + \eta \nabla^2 \mathbf{B}, \quad (31)$$

with $\eta = c^2/4\pi\sigma$ being the magnetic diffusivity. The first term on the right-hand side is called the convective term, while the second term is called the diffusive term. Depending on the value of the Reynolds number R_m , which gives the ratio of the convective term ($\propto v_0 B_0/l_0$) to the diffusive term ($\propto \eta B_0/l_0^2$),

$$R_m = \frac{l_0 v_0}{\eta}, \quad (32)$$

the induction equation can be approximated in the two limits by

$$\frac{d\mathbf{B}}{dt} \approx \nabla \times (\mathbf{v} \times \mathbf{B}) \quad \text{for } R_m \gg 1 \quad (33)$$

$$\frac{d\mathbf{B}}{dt} \approx \eta \nabla^2 \mathbf{B} \quad \text{for } R_m \ll 1 \quad (34)$$

The plasma in the solar corona is close to a perfectly conducting medium (with a high Reynolds number $R_m \approx 10^8 - 10^{12}$), so that approximation (Eq. 33) with $R_m \gg 1$ applies, while the diffusive limit (Eq. 34) with $R_m \ll 1$ is not relevant. Thus, cross-field diffusion is generally inhibited in the solar corona.

While cross-field transport is generally inhibited in low plasma- β parameter regions, it can be enabled by gyro-orbit perturbations due to local magnetic field fluctuations, a process called Rechester-Rosenbluth diffusion (Galloway et al. 2006), but this process is estimated to operate on time scales of days, and thus is way too slow to explain the observed anomalous diffusion in flares. A scenario with small-scale random footpoint motion that injects energy into the corona by twisting and braiding was invoked as a coronal heating mechanism, where helicity conservation leads to hyper-diffusion (VanBallegooijen and Cranmer 2008), but this is also driven by photospheric diffusion speeds, and thus not fast enough to drive solar flares.

4.4. Diffusion Processes in Solar Flares

Let us discuss first diffusion processes in the preflare phase. Resistive diffusion of force-free magnetic fields has been considered to develop infinite field gradients and to trigger the eruption of solar flares (Low 1973a,b; 1974b) and acceleration of particles (Low 1974a). On the other side, photospheric diffusion is thought to reduce the non-potential magnetic (free) energy that is built up by the photospheric shearing motion (Wu et al. 1992). The eruption of a coronal mass ejection (CME) was simulated with MHD simulations, where slow turbulent diffusion of the footpoints of coronal magnetic field lines leads to a loss of equilibrium and drives the eruption (Amari et al. 2003). However, all these diffusion processes occur before a flare, and thus do not explain the rapid diffusion during flares.

What happens during flares? The driving instability of solar flares is generally linked to the dynamics of magnetic reconnection processes. Diffusion of particles is most efficient in the X-point of collisionless magnetic reconnection regions, where the magnetic field drops to zero. This diffusion region is subject of numerous theoretical and simulation studies (e.g., see review by Hesse et al. 2011). The duration of a magnetic reconnection process is approximately the Alfvénic transit time across a coronal reconnection region, which is of order $T_1 = L/v_A \approx 10$ s (for $L = 10,000$ km and $v_A = 1000$ km s $^{-1}$). While such a single magnetic reconnection episode (Sweet-Parker-type or Petschek-type) can only explain very short single-loop flares, large flares (with a range of durations $T = 120 - 8460$ s observed here) require a chain reaction of magnetic reconnection events, perhaps in the order of $N = T/T_1 = 12 - 850$ reconnection episodes. Evidence for such multi-reconnection events has been demonstrated for numerous large flares, the most prominent case being the Bastille-Day flare, where over $N \gtrsim 200$ postflare loops have been traced, probably each one being a remnant of a local magnetic reconnection process (e.g., Aschwanden and Alexander 2001), forming a multi-loop postflare configuration (Hori et al. 1998). Theoretical models of multi-reconnection or intermittent, unsteady, bursty reconnection have also been formulated in terms of the tearing mode instability and coalescence instability, and combinations of both (e.g., Furth et al. 1963; Sturrock 1996; Kliem 1990, 1995; Leboef et al. 1982; Tajima et al. 1982; Karpen et al. 1995; Kliem et al. 2000; Drake et al. 2009). The question is now how the time evolution of such an intermittent chain reaction of magnetic reconnection episodes ties into our simplified diffusion evolutionary model.

Perhaps our measurements of the average expansion speed can give us a hint about the physical mechanism of the diffusion process. We measured average speeds in the range of $v = 3 - 103$ km s $^{-1}$, and maximum speeds of $v_{max} = 8 - 550$ km s $^{-1}$. If we assume typical plasma temperatures of $T \approx 10 - 30$ MK for the observed large (M and X-class) flares, we expect sound speeds of $c_s \approx 166\sqrt{T_{MK}} \approx 500 - 900$ km s $^{-1}$, which are about 1-2 orders of magnitude faster than the observed speeds. Therefore, the diffusive speed we observe in these large flares cannot just be the propagation speed of upflowing plasma into and along flare loops initiated by the chromospheric evaporation process, which occurs approximately with sound speed. There are some additional delays that intervene between the subsequent filling of individual loops in a flare

arcade. A model where subsequent flare loops are triggered by a slow (acoustic) wave that propagates at some angle ($25^\circ - 28^\circ$) along the arcade was proposed by Nakariakov and Zimovets (2011) and tested by the timing of the hard X-ray footpoints (Inglis and Dennis 2012), but the predicted hard X-ray pulse periods did not agree with the observed ones. Nevertheless, the mean footpoint speed found in the analyzed three flares ($v = 5 - 60 \text{ km s}^{-1}$; Inglis and Dennis 2012) is similar to our observed range ($v = 3 - 103 \text{ km s}^{-1}$), which corroborates the congruence between the magnetic reconnection path and the hard X-ray footpoint path. Similar propagation speeds of the hard X-ray footpoints were also measured along an arcade of flare loops by Grigis and Benz (2005), i.e., a mean velocity of $v = 63 - 65 \text{ km s}^{-1}$ parallel to the arcade, with a peak speed of about $v = 110 \text{ km s}^{-1}$ for 2 minutes. Hence we can interpret our diffusion speed as mean propagation speed of subsequently triggered magnetic reconnection sites.

The measurement of the spatio-temporal evolution during solar flares should also ameliorate estimates of the *particle number problem* (Brown and Melrose 1977), which requires the knowledge of the flare volume and its temporal change and spatial propagation path.

4.5. Fractal Diffusion, Sub-Diffusion, or Logistic Growth ?

We combined the different anomalous and classical diffusion models into a single framework (Eq. 24) that has only one single parameter (β) that discriminates between the different models: $\beta = 0$ is the limit of logistic growth, $\beta = 0 - 1$ is the sub-diffusive regime, $\beta = 1$ is classical diffusion or Brownian motion, $\beta = 1 - 2$ is the super-diffusive regime or Lévy flights, and $\beta = 2$ is the limit of linear expansion. Our results yielded a range of $\beta = 0.04 - 1.35$ that covers three of these regimes, but the majority is found in the sub-diffusive regime with a mean and standard deviation of $\beta = 0.53 \pm 0.27$. What does this mean and why is it different from the classical diffusion model based on random walk?

Brownian motion or classical diffusion is based on homogeneous isotropic expansion. In solar flares, as well as in cellular automaton models, however, the medium is inhomogeneous (which can be characterized by a fractal dimension). The solar corona, moreover, is highly anisotropic due to the structuring by the magnetic field (in the low plasma- β regime), which also applies to flares, except to a reduced degree in the diffusion regions of magnetic X-point reconnection configurations. Let us assume the extreme case where plasma can only flow in one direction along magnetic fluxtubes. The anisotropic volume increase will scale as $V(t) \propto r(t)$, instead of $V(t) \propto r^3$ in an isotropic medium. The observable area $A(t)$ will then grow only in one direction (say in x -direction) with a constant width (say Δy),

$$A_{iso}(t) = x_{iso}(t)\Delta y, \tag{35}$$

and the derived flare expansion radius $r(t) = \sqrt{A(t)/\pi}$ will scale as

$$r(t) = \sqrt{\frac{A_{iso}(t)}{\pi}} \propto x_{iso}(t)^{1/2} \propto t^{1/4}, \tag{36}$$

for a classical diffusion process in one dimension, i.e., $x_{iso}(t) \propto t^{1/2}$. Thus by defining anomalous diffusion by $r(t) \propto t^{\beta/2}$ we end up with a diffusion index of $\beta = 1/2$, which is indicative of the sub-diffusive regime. Now, although the electron and ion diffusion region in magnetic reconnection X-points allow 2-D or 3-D diffusion, our observational result of sub-diffusion with $\beta \approx 1/2$ suggests that the triggering of subsequent magnetic reconnection episodes occurs along anisotropic 1-D paths and dominates the overall diffusion of the flare process, regardless of the near-isotropic diffusion regions in X-points.

What does the extreme limit of logistic growth mean, where the diffusion comes to a halt at some time near the peak time of the flare and does not expand further. Apparently, the energy release process approaches regions with strong magnetic fields that are stable and not prone to magnetic reconnection, so that the chain reaction of reconnection episodes does not propagate further, while energy release in the previous area still continues. It is like a domino chain reaction that hits the wall of a room. The domino effect can still propagate in the unstable regions inside the room, but cannot expand outside of the room. Alternatively, the progressing flare could also reach the boundary of an active region, where only weak-field regions of the Quiet Sun are available which harbour much less non-potential magnetic energy than the inside of active regions.

In summary, the diffusion index β tells us some interesting information about the anisotropy and boundaries of magnetic topologies in solar flare regions.

5. CONCLUSIONS

We analyzed the spatio-temporal evolution in the 155 largest solar flares (M and X-class) observed by GOES and AIA/SDO during the first two years of the SDO mission. We fitted the radial expansion $r(t)$ of flare areas detected in the 335 Å filter above some threshold level with a generalized diffusion model that includes the classical diffusion, anomalous diffusion, and the logistic growth limit. The major results and conclusions are:

1. The flare area in all events can be fitted with a radial expansion model $r(t)$ that consists of an initial acceleration phase with exponential growth and a deceleration phase that follows anomalous diffusion, $r(t) \propto \kappa t^{\beta/2}$, with $\beta = 0.53 \pm 0.27$ mostly falling into the sub-diffusive regime. The most extreme cases range from logistic growth ($\beta = 0.04$) to super-diffusion ($\beta = 1.35$). The sub-diffusive characteristics is likely to reflect the anisotropic propagation of energy release in a magnetically dominated plasma. The limit of logistic growth indicates the times when the boundaries of energy release regions are reached.
2. The diffusion coefficient $\kappa = 53 \pm 23 \text{ km s}^{-\delta/2}$, which corresponds to an area diffusion constant of $D \approx 300 - 1600 \text{ km}^2 \text{ s}^{-1}$ is found to be significantly faster than diffusion processes measured in the photosphere ($D \approx 100 - 600 \text{ km s}^{-1}$) and cannot be explained with crossfield diffusion in the corona, which is strongly inhibited by the low plasma- β parameter.
3. The average diffusion speed during flares is measured in the range of $v \approx 5 - 100 \text{ km s}^{-1}$, with maximum speeds of $v_{max} \approx 10 - 500 \text{ km s}^{-1}$, which is slower than the sound speed of $c_s \approx 500 - 900 \text{ km s}^{-1}$ expected in flares with temperatures of $T_e \approx 10 - 30 \text{ MK}$, but is compatible with the hard X-ray footpoint motion along the neutral line during flares, and thus is likely to represent the mean propagation speed of subsequently triggered magnetic reconnection sites.
4. The fractal-diffusive self-organized criticality model (FD-SOC) describes the diffusive flare progression in a fractal geometry and predicts powerlaw distributions with slopes of $\alpha_L = 3.0$ for length scales L , $\alpha_T = 1.1 - 2.0$ for time scales T , and $\alpha_P = 1.83$ for peak fluxes P , based on the observed diffusion index range of $\beta \approx 0.1 - 1.0$, the observed flux-volume scaling of $F_{335} \propto (dV/dt)^{0.8}$, in a 3D-space geometry with fractal dimension $D_3 = 2.0$. Our observations yield $\alpha_L = 2.0$, $\alpha_T = 2.2$, and $\alpha_P = 1.34$, which is not inconsistent with the FD-SOC model, given the large uncertainties of the powerlaw slopes determined in a small statistical sample. Nevertheless, the evolutionary fits $r(t) \propto t^{\beta/2}$ of individual

flares confirm the diffusive property of the FD-SOC model for the case of solar flares with a high degree of accuracy, which has been previously predicted based on cellular automaton simulations.

Thus, the major accomplishment of this study is the experimental proof of a diffusive flare expansion process that has been predicted by the fractal-diffusive self-organized criticality (FD-SOC) model. However, while the classical FD-SOC model assumed classical diffusion ($\beta = 1$), the observational results from AIA/SDO revealed mostly sub-diffusion ($\beta \lesssim 1$), down to the limit of logistic growth ($\beta \gtrsim 0$). Future studies may extend the statistics of spatio-temporal parameters and allow us to test the predicted size distributions of SOC models with higher accuracy and establish physical scaling laws for flares that are based on the fundamental geometric parameters of space and time.

The author acknowledges helpful discussions and software support of the AIA/SDO team. This work was partially supported by NASA contract NNX11A099G “Self-organized criticality in solar physics” and NASA contract NNG04EA00C of the SDO/AIA instrument to LMSAL.

Appendix A: Generalized Fractal-Diffusive Self-Organized Criticality Model

We generalize the *fractal-diffusive self-organized criticality model (FD-SOC)* described in Aschwanden (2012) in two respects, (1) regarding anomalous diffusion, and (2) for arbitrary (wavelength-dependent) flux-volume scaling. In the original FD-SOC model, classical diffusion was assumed, i.e., a scaling of $L \propto T^{1/2}$ between the length scale L and time duration T , which we generalize for anomalous diffusion (with diffusion index β),

$$L \propto T^{\beta/2} . \quad (A1)$$

which includes also the case of classical diffusion ($\beta = 1$). The second generalization is the the scaling of an observed flux F_λ in a given wavelength λ to the emissive volume rate of change dV_S/dt ,

$$F_\lambda \approx \left(\frac{dV_S}{dt} \right)^\gamma , \quad (A2)$$

where $\gamma = 1$ was assumed to be unity in the original FD-SOC model, but can now be wavelength-dependent and accomodate some astrophysical scaling law of the underlying emission and absorption process at wavelength λ .

The FD-SOC model describes the inhomogeneity of SOC avalanches with a fractal structure with Hausdorff dimension D_S in Euclidean space with dimension S . The instantaneous avalanche volume dV_S/dt is then characterized by

$$\frac{dV_S}{dt} \propto L^{D_S} , \quad (A3)$$

and the mean fractal dimension D_S can be estimated from the arithmetic mean of the minimum and maximum possible value,

$$D_S \approx \frac{(1 + S)}{2} , \quad (A4)$$

yielding a mean value of $D_3 = 2.0$ for the 3D Euclidean space ($S = 3$). Combining Eqs. (A1-A3) yields then the correlation of the instantaneous energy dissipation volume (dV_S/dt) and the time duration T ,

$$F_\lambda \propto \left(\frac{dV_S}{dt} \right)^\gamma \propto L^{D_S \gamma} \propto T^{D_S \gamma \beta/2} . \quad (A5)$$

This flux quantity F_λ is generally strongly fluctuating, and the peak dissipation rate $P_\lambda = \max(F_\lambda)$ can be estimated from the maximum fractal dimension $D_S \lesssim S$,

$$P_\lambda \propto \left(\frac{dV_S}{dt} \right)^\gamma \propto L^{S\gamma} \propto T^{S\gamma\beta/2}. \quad (A6)$$

A more steady quantity is the time-integrated volume V_S of a SOC avalanche, which can be obtained from the time-integration of the instantaneous volume rate of change (dV_S/dt), and be associated with the fluence E_λ (or time-integrated flux $E_\lambda = \int F_\lambda(t)dt$),

$$E_\lambda \propto \int_0^T F_\lambda(t) dt \propto \int_0^T t^{D_S\gamma\beta/2} dt \propto T^{1+(D_S\gamma\beta/2)}. \quad (A7)$$

After we obtained the scaling between the parameters $L, T, F_\lambda, P_\lambda$, and E_λ , we can calculate the powerlaw slopes of their size distributions. The basic reference is the distribution function $N(L)$ of spatial scales, which be reciprocal to the size in a slowly-driven homogeneous SOC system that is scale-free and where avalanches can occur in any size. The relative probability is then (Aschwanden 2012),

$$N(L) \propto V_S^{-1} \propto L^{-S}. \quad (A8)$$

All other frequency distributions can then be derived by substituting the corresponding parameter correlations given in Eq. (A1-A7), First we can calculate the occurrence frequency distribution of avalanche time scales, by using the diffusive boundary propagation relationship $L(T) \propto T^{\beta/2}$ (Eq. A1), by substituting the variable T for L in the distribution $N(L)$ (Eq. A8),

$$N(T)dT = N(L[T]) \left| \frac{dL}{dT} \right| dT \propto T^{-[1+(S-1)\beta/2]} dT. \quad (A9)$$

Subsequently we can derive the occurrence frequency distribution function $N(F)$ for the instantaneous energy dissipation rate F using the relationship $F_\lambda(T) \propto T^{D_S\gamma\beta/2}$ (Eq. A5),

$$N(F_\lambda)dF_\lambda = N(T[F_\lambda]) \left| \frac{dT}{dF_\lambda} \right| dF_\lambda \propto F_\lambda^{-[1+(S-1)/D_S\gamma]} dF_\lambda, \quad (A10)$$

the occurrence frequency distribution function of the peak energy dissipation rate P using the relationship $P_\lambda(T) \propto T^{S\gamma\beta/2}$ (Eq. A6),

$$N(P_\lambda)dP_\lambda = N(T[P_\lambda]) \left| \frac{dT}{dP_\lambda} \right| dP_\lambda \propto P_\lambda^{-[1+(S-1)/S\gamma]} dP_\lambda, \quad (A11)$$

and the occurrence frequency distribution function $N(E_\lambda)$ for the total energy E_λ using the relationship $E_\lambda(T) \propto T^{(1+D_S\gamma\beta/2)}$ (Eq. A7),

$$N(E_\lambda)dE_\lambda = N(T[E_\lambda]) \left| \frac{dT}{dE_\lambda} \right| dE_\lambda \propto E_\lambda^{-[1+(S-1)/(D_S\gamma+2/\beta)]} dE_\lambda. \quad (A12)$$

This derivation yields naturally powerlaw functions for all parameters $L, T, F_\lambda, P_\lambda$, and E_λ , which are the hallmarks of SOC systems. In summary, if we denote the occurrence frequency distributions $N(x)$ of a parameter x with a powerlaw distribution with power index α_x ,

$$N(x)dx \propto x^{-\alpha_x} dx, \quad (A13)$$

we have the following powerlaw coefficients α_x for the parameters $x = L, T, F_\lambda, P_\lambda$, and E_λ ,

$$\begin{aligned}
 \alpha_L &= S \\
 \alpha_T &= 1 + (S - 1)\beta/2 \\
 \alpha_F &= 1 + (S - 1)/(D_S\gamma) \\
 \alpha_P &= 1 + (S - 1)/(S\gamma) \\
 \alpha_E &= 1 + (S - 1)/(D_S\gamma + 2/\beta)
 \end{aligned}
 \tag{A14}$$

Note, that the powerlaw slopes α_L , α_F and α_P do not depend on the diffusion index β , and thus are identical for classical or anomalous diffusion, while α_T and α_E depend on the diffusion index β .

REFERENCES

- Abramenko, V.I., Carbone, V., Yurchyshyn, V., Goode, P.R., Stein, R.F., Lepreti, F., Capparelli, V., and Vecchio, A. 2011, *ApJ*, 743, 133.
- Amari, T., Luciani, J.F., Aly, J.J., Mikic, Z., and Linker, J. 2003, *ApJ*, 595, 1231.
- Aschwanden, M.J., Wills, M.J., Hudson, H.S., Kosugi, T., and Schwartz, R.A. 1996, *ApJ*, 468, 398.
- Aschwanden, M.J., Dennis, B.R., and Benz, A.O. 1998, *ApJ*, 497, 972.
- Aschwanden, M.J. 1999, *Sol. Phys.*, 190, 233.
- Aschwanden, M.J., Tarbell, T., Nightingale, R., Schrijver, C.J., Title, A., Kankelborg, C.C., Martens, P.C.H., and Warren, H.P. 2000, *ApJ*, 535, 1047.
- Aschwanden, M.J. and Alexander, D. 2001, *Sol. Phys.*, 204, 91.
- Aschwanden, M.J. and Parnell, C.E. 2002, *ApJ*, 572, 1048.
- Aschwanden, M.J. and Aschwanden, P.D. 2008a, *ApJ*, 674, 530.
- Aschwanden, M.J. and Aschwanden, P.D. 2008b, *ApJ*, 674, 544.
- Aschwanden, M.J. 2011, *Self-Organized Criticality in Astrophysics. The Statistics of Nonlinear Processes in the Universe*, ISBN 978-3-642-15000-5, Springer-Praxis: New York, 416p.
- Aschwanden, M.J. 2012, *A&A*, 539, A2.
- Aschwanden, M.J. and Freeland, S.L. 2002, *ApJ*, 755, (in press).
- Bak, P., Tang, C., and Wiesenfeld, K. 1987, *Physical Review Lett.* 59/27, 381.
- Beltrami, E. 1987, *Mathematics for dynamic modeling*, Academic Press, Inc.: Boston.
- Berghmans, D., Clette, F., and Moses, D. 1998, *A&A*, 336, 1039.
- Bregman, M. 2007, *Planet. Space Sci.* 55/15, 2228.
- Bregman, M. 2008, *Physica A*, 387/10, 2328.
- Brown, R. 1828, *Phil. Mag.* 4, 161.
- Brown, J.C., and Melrose, D.B. 1977, *Sol. Phys.*, 52, 117.
- Drake, J.F., Cassak, P.A., Shay, M.A., Swisdak, M., and Quataert, E. 2009, *ApJ*, 700, L16.
- Earnshaw, R.C. and Riley, E.M. 2011, *Brownian Motion. Theory, Modelling and Applications*, ISBN 978-1-61209-537-0, Nova Science Publishers.
- Einstein, A. 1905, *Ann. Physik* 17, 549.

- Furth, H.P., Killeen, J., and Rosenbluth, M.N. 1963, *Phys.Fluids* 6, 459.
- Galloway, R.K., Helander, P., MacKinnon, A.L. 2006, *ApJ*, 646, 615.
- Garcia H. A.: 1998, *ApJ*, 504, 1051.
- Grigis, P.C. and Benz, A.O. 2005, *ApJ*, 625, L143.
- Grigolini, P., Leddon, D., and Scafetta, N. 2002, *Phys. Rev. E* 65/4, id. 046203.
- Hesse, M., Neukirch, T., Schindler, K., Kuznetsova, M. and Zenitani, S. 2011, *Space Sci.Rev.* 160, 3.
- Hori, K., Yokoyama, T., Kosugi, T., and Shibata, K. 1998, *ApJ*, 500, 492.
- Inglis, A.R. and Dennis, B.R. 2012, *ApJ*, 748, id. 139.
- Jackson, E.A. 1989, *Perspectives of nonlinear dynamics*, Cambridge University Press: Cambridge.
- Kankelborg, C.C., Walker, A.B.C.II, and Hoover, R.B. 1997, *ApJ*, 491, 952.
- Kano,R. and Tsuneta,S. 1995 *ApJ*, 454, 934.
- Karpen, J.T., Antiochos, S.K., DeVore, C.R., and Golub, L. 1998, *ApJ*, 495, 491.
- Kliem, B. 1990, *Astron.Nachr.* 311/6, 399.
- Kliem, B., Karlicky, M., and Benz, A.O. 2000, *A&A*, 360, 715.
- Komm, R.W., Howard, R.F., and Harvey, J.W. 1995, *Sol. Phys.*, 158, 213.
- Krucker, S. and Benz, A.O. 1998, *ApJ*, 501, L213.
- Lawrence, J.K. 1991, *Sol. Phys.*, 135, 249.
- Leboef, J.N., Tajima, T., and Dawson,J.M. 1982, *Phus.Fluids* 25, 784.
- Leighton R.B. 1964, *ApJ*, 140, 1547.
- Leighton R.B. 1969, *ApJ*, 156, 1.
- Lemen, J.R. et al. 2012, *Sol. Phys.*, 275, 17.
- Litvinenko, Y.E. 2011, *ApJ*, 731, L39.
- Low, B.C. 1973a, *ApJ*, 181, 209.
- Low, B.C. 1973b, *ApJ*, 184, 917.
- Low, B.C. 1974a, *ApJ*, 189, 353.
- Low, B.C. 1974b, *ApJ*, 193, 243.
- Lu, E.T., and Hamilton, R.J. 1993, *ApJ*, 380, L89.
- Mandelbrot, B.B. 1982, *The Fractal Geometry of Nature*, ISBN 0-7167-186-9, W.H. Freeman.
- May R.M. 1974. *Model Ecosystems*, Princeton: Princeton New Jersey.
- Metcalf,T.R. and Fisher,G.H.: 1996, *apj*, 462, 977.
- Mosher, J.M. 1977, PhD Thesis, California Inst. Techn., Pasadena CA.
- Nagashima, K. and Yokoyama, T. 2006, *ApJ*, 647, 654.
- Nakariakov, V.M. and Zimovets, I.V. 2011, *ApJ*, 730, L27.
- Pallavicini, R., Serio, S., and Vaiana, G.S. 1977, *ApJ*, 216, 108.
- Perlmutter, S. et al. 1999, *ApJ*, 517, 565.
- Porter,L.J. and Klimchuk,J.A. 1995 *ApJ*, 454, 499.

- Reale,F, Betta,R., Peres,G., Serio,S., and McTiernan,J. 1997, A&A, 325, 782.
- Riess, A. et al. 1998, AJ, 116, 1009.
- Riess, A.G. et al. 2004, ApJ, 607, 665.
- Ruzmaikin, A.A., Cadavid, A.C., Chapman, G.A., Lawrence, J.K., and Walton, S.R. 1996, ApJ471, 1022.
- Schrijver, C.J. and Marin, S.F. 1990, Sol. Phys., 129, 95.
- Schrijver, C.J., Shine, R.A., Hagenaar, H.J., Strous, L.H., Jefferies, S.M., Jones, A.R., Harvey, J.W., and Duvall, T.L.Jr. 1996, ApJ, 468, 921.
- Shimizu,T.: 1997, PhD. Thesis, Natl.Astron.Observatory, Mitaka, Tokyo 181, Japan.
- Sturrock, P.A. 1966, Nature 5050, 695.
- Tajima,T., Brunel,F. and Sakai,J. 1982, ApJ, 258, L45.
- VanBallegooijen, A.A. and Cranmer, S.R. 2008, ApJ, 682, 644.
- Wang, Y.M., Nash, A.G., and Sheeley, N.R. 1989, Science 245, 712.
- Wang, H.N., Cui, Y.M., and He, H. 2009, Res. Astron. Astroph. 9, 687.
- Wu, S.T., Yin,C.L., and Yang, W.H. 1992, Sol. Phys., 142, 313.
- Zirin, H. 1985, ApJ, 291, 858.
- Zumofen,G., Klafter, J., and Shlesinger, M.F. 1999, Lecture Notes in Physics, Vol. 519, ISBN 978-3-540-65416-2, Springer: Berlin.

Table 1. Catalog of analyzed M and X-class flare events and best-fit model parameters: length scale L (Mm), diffusion coefficient κ ($\text{km s}^{-\beta/2}$), diffusion index β , and goodness-of-fit q_{fit} .

Nr	Observation date	Start time	Peak time	End time	Duration T(s)	GOES class	NOAA AR	Heliogr. position	Length L(Mm)	Diff. coeff. κ	Diff. index β	Fit q_{fit}
1	2010-06-12	00:30	00:57	01:02	1920	M2.0	11081	N23W47	12	65±25	0.60±0.27	2.9%
2	2010-06-13	05:30	05:39	05:44	840	M1.0	11079	S24W82	8	35± 4	0.81±0.11	1.8%
3	2010-08-07	17:55	18:24	18:47	3120	M1.0	11093	N14E37	40	107± 4	0.36±0.02	2.2%
4	2010-10-16	19:07	19:12	19:15	480	M2.9	11112	S20W26	17	86±18	0.55±0.03	2.6%
5	2010-11-04	23:30	23:58	00:12	2520	M1.6	11121	S20E85	12	34± 0	0.23±0.05	1.9%
6	2010-11-05	12:43	13:29	14:06	4980	M1.0	11121	S20E75	14	38± 2	0.58±0.06	1.6%
7	2010-11-06	15:27	15:36	15:44	1020	M5.4	11121	S20E58	14	68± 6	0.53±0.01	1.7%
8	2011-01-28	00:44	01:03	01:10	1560	M1.3	11149	N16W88	11	30± 2	0.12±0.06	3.3%
9	2011-02-09	01:23	01:31	01:35	720	M1.9	11153	N16W70	14	46±12	0.23±0.09	3.4%
10	2011-02-13	17:28	17:38	17:47	1140	M6.6	11158	S20E05	21	74±12	0.46±0.04	2.6%
11	2011-02-14	17:20	17:26	17:32	720	M2.2	11158	S20E04	23	66±11	0.15±0.01	2.2%
12	2011-02-15	01:44	01:56	02:06	1320	X2.2	11158	S20W10	33	114± 3	0.66±0.28	2.9%
13	2011-02-16	01:32	01:39	01:46	840	M1.0	11158	S20W24	12	46± 5	0.56±0.04	2.5%
14	2011-02-16	07:35	07:44	07:55	1200	M1.1	11161	S19W29	10	41± 4	0.66±0.01	2.5%
15	2011-02-16	14:19	14:25	14:29	600	M1.6	11158	S21W30	16	41± 4	0.10±0.01	1.1%
16	2011-02-18	09:55	10:11	10:15	1200	M6.6	11158	S21W55	13	81±13	0.57±0.05	4.2%
17	2011-02-18	10:23	10:26	10:37	840	M1.0	11162	N22E10	14	41± 4	0.25±0.03	2.6%
18	2011-02-18	12:59	13:03	13:06	420	M1.4	11158	S20W70	7	47± 5	0.81±0.03	1.8%
19	2011-02-18	14:00	14:08	14:15	900	M1.0	11162	N22E10	14	40± 5	0.17±0.00	2.0%
20	2011-02-18	20:56	21:04	21:14	1080	M1.3	11162	N22E10	9	48± 2	0.81±0.09	1.8%
21	2011-02-24	07:23	07:35	07:42	1140	M3.5	11163	N14E87	17	77±17	0.88±0.12	2.5%
22	2011-02-28	12:38	12:52	13:03	1500	M1.1	11164	N28E39	20	55± 6	0.28±0.02	2.3%
23	2011-03-07	05:00	05:13	05:19	1140	M1.2	11164	N23E47	21	71±11	0.58±0.03	2.2%
24	2011-03-07	07:49	07:54	07:56	420	M1.5	11165	S18W75	9	38±15	0.34±0.19	2.7%
25	2011-03-07	07:59	08:07	08:15	960	M1.4	11164	N27W46	23	63± 6	0.18±0.02	2.0%
26	2011-03-07	09:14	09:20	09:28	840	M1.8	11164	S17W77	5	31±15	0.92±0.33	3.0%
27	2011-03-07	13:45	14:30	14:56	4260	M1.9	11166	N11E21	30	72± 6	0.42±0.04	2.1%
28	2011-03-07	19:43	20:12	20:58	4500	M3.7	11164	N30W48	51	117±10	0.47±0.08	1.2%
29	2011-03-07	21:45	21:50	21:55	600	M1.5	11165	S17W82	10	25± 1	0.10±0.01	2.0%
30	2011-03-08	02:24	02:29	02:32	480	M1.3	11165	S18W80	9	27± 3	0.26±0.03	2.0%
31	2011-03-08	03:37	03:58	04:20	2580	M1.5	11171	S21E72	32	90± 5	0.79±0.07	1.7%
32	2011-03-08	10:35	10:44	10:55	1200	M5.3	11165	S17W88	19	59± 9	0.38±0.03	3.3%
33	2011-03-08	18:08	18:28	18:41	1980	M4.4	11165	S17W88	13	37± 7	0.52±0.15	2.7%
34	2011-03-08	19:46	20:16	21:19	5580	M1.4	11165	N23W43	26	60± 3	0.50±0.09	2.0%
35	2011-03-09	10:35	11:07	11:21	2760	M1.7	11166	N08W11	21	56± 6	0.63±0.04	3.2%
36	2011-03-09	13:17	14:02	14:13	3360	M1.7	11166	S26W78	12	27± 7	0.73±0.12	2.8%
37	2011-03-09	23:13	23:23	23:29	960	X1.5	11166	N08W11	34	123±17	0.56±0.03	1.9%
38	2011-03-10	22:34	22:41	22:49	900	M1.1	11166	N08W25	8	42±10	1.14±0.01	2.3%
39	2011-03-12	04:33	04:43	04:48	900	M1.3	11166	N07W35	16	53± 9	0.35±0.03	1.7%
40	2011-03-14	19:30	19:52	19:54	1440	M4.2	11169	N16W49	17	54± 6	0.26±0.04	3.4%
41	2011-03-15	00:18	00:22	00:24	360	M1.0	11169	N11W83	9	27± 5	0.17±0.06	2.7%
42	2011-03-23	02:03	02:17	02:24	1260	M1.4	11176	S25W84	18	58± 8	0.45±0.02	1.4%
43	2011-03-24	12:01	12:07	12:11	600	M1.0	11176	S15E43	15	48± 5	0.26±0.03	2.3%
44	2011-03-25	23:08	23:22	23:30	1320	M1.0	11176	S12E26	20	59± 2	0.39±0.06	1.9%
45	2011-04-15	17:02	17:12	17:28	1560	M1.3	11190	N13W24	13	43± 6	0.42±0.04	1.4%
46	2011-04-22	04:35	04:57	05:14	2340	M1.8	11195	S17E42	20	60±12	0.77±0.14	2.0%
47	2011-04-22	15:47	15:53	16:11	1440	M1.2	11195	S18E36	20	57± 5	0.36±0.03	1.5%

Table 1—Continued

Nr	Observation date	Start time	Peak time	End time	Duration T(s)	GOES class	NOAA AR	Heliogr. position	Length L(Mm)	Diff. coeff. κ	Diff. index β	Fit q_{fit}
48	2011-05-28	21:09	21:50	22:01	3120	M1.1	11226	S21E70	14	37± 5	0.72±0.08	1.9%
49	2011-05-29	10:08	10:33	11:08	3600	M1.4	11226	S20E64	24	68± 6	0.93±0.14	2.5%
50	2011-06-07	06:16	06:41	06:59	2580	M2.5	11226	S22W53	33	85± 7	0.30±0.02	1.5%
51	2011-06-14	21:36	21:47	22:10	2040	M1.3	11236	N14E77	20	55± 4	0.37±0.02	1.7%
52	2011-07-27	15:48	16:07	16:22	2040	M1.1	11260	N19E38	19	63± 8	0.55±0.15	2.7%
53	2011-07-30	02:04	02:09	02:12	480	M9.3	11261	N14E35	26	139±20	0.62±0.01	2.7%
54	2011-08-02	05:19	06:19	06:48	5340	M1.4	11261	N17W12	28	74± 7	0.68±0.05	1.7%
55	2011-08-03	03:08	03:37	03:51	2580	M1.1	11261	N15W28	13	37± 4	0.24±0.06	2.6%
56	2011-08-03	04:29	04:32	04:35	360	M1.7	11263	N16E10	21	73± 7	0.29±0.01	1.0%
57	2011-08-03	13:17	13:48	14:10	3180	M6.0	11261	N17W30	28	78± 3	0.72±0.04	3.0%
58	2011-08-04	03:41	03:57	04:04	1380	M9.3	11261	N16W38	32	92±16	0.28±0.02	1.9%
59	2011-08-08	18:00	18:10	18:18	1080	M3.5	11263	N15W62	17	57± 6	0.47±0.01	1.5%
60	2011-08-09	03:19	03:54	04:08	2940	M2.5	11263	N17W69	12	39± 5	1.35±0.03	2.1%
61	2011-08-09	07:48	08:05	08:08	1200	X6.9	11263	N14W69	29	95±12	0.19±0.00	3.2%
62	2011-09-04	11:21	11:45	11:50	1740	M3.2	11286	N18W84	10	38± 1	0.50±0.14	3.3%
63	2011-09-05	04:08	04:28	04:32	1440	M1.6	11286	N18W87	13	46± 0	0.55±0.12	2.0%
64	2011-09-05	07:27	07:58	08:06	2340	M1.2	11286	N18W87	7	22± 2	1.33±0.29	2.3%
65	2011-09-06	01:35	01:50	02:05	1800	M5.3	11283	N13W07	21	60± 8	0.37±0.05	0.9%
66	2011-09-06	22:12	22:20	22:24	720	X2.1	11283	N14W18	29	87± 6	0.18±0.03	3.4%
67	2011-09-07	22:32	22:38	22:44	720	X1.8	11283	N14W31	36	101±15	0.17±0.02	1.2%
68	2011-09-08	15:32	15:46	15:52	1200	M6.7	11283	N14W41	27	80±14	0.32±0.08	1.8%
69	2011-09-09	06:01	06:11	06:17	960	M2.7	11283	N14W48	16	73±21	0.85±0.30	1.8%
70	2011-09-09	12:39	12:49	12:56	1020	M1.2	11283	N15W50	15	45± 5	0.35±0.01	1.1%
71	2011-09-10	07:18	07:40	07:56	2280	M1.1	11283	N14W64	15	47± 6	0.91±0.02	1.0%
72	2011-09-21	12:04	12:23	12:45	2460	M1.8	11301	N15E88	6	18± 3	0.48±0.03	2.6%
73	2011-09-22	09:53	10:00	10:09	960	M1.1	11302	N24W55	12	52± 9	0.87±0.04	3.1%
74	2011-09-22	10:29	11:01	11:44	4500	X1.4	11302	N08E89	41	85± 5	0.99±0.13	1.3%
75	2011-09-23	01:47	01:59	02:10	1380	M1.6	11295	N24W64	14	59±10	1.20±0.02	2.3%
76	2011-09-23	21:54	22:15	22:34	2400	M1.6	11295	N12E56	17	52± 5	0.72±0.08	2.1%
77	2011-09-23	23:48	23:56	00:04	960	M1.9	11302	N12E56	23	69±12	0.32±0.03	2.0%
78	2011-09-24	09:21	09:40	09:48	1620	X1.9	11302	N13E61	23	60± 9	0.16±0.02	2.6%
79	2011-09-24	12:33	13:20	14:10	5820	M7.1	11302	N15E59	39	80± 9	1.05±0.11	2.0%
80	2011-09-24	16:36	16:59	17:15	2340	M1.7	11295	N23W87	12	42± 4	1.07±0.07	1.2%
81	2011-09-24	17:19	17:25	17:31	720	M3.1	11302	N13E54	8	35± 9	0.79±0.17	3.1%
82	2011-09-24	17:59	18:15	18:24	1500	M2.8	11302	N13E56	18	46± 7	0.16±0.01	1.4%
83	2011-09-24	19:09	19:21	19:41	1920	M3.0	11302	N12E42	26	78± 8	0.74±0.02	1.8%
84	2011-09-24	20:29	20:36	20:42	780	M5.8	11302	N13E52	11	47± 9	0.55±0.03	3.8%
85	2011-09-24	21:23	21:27	21:32	540	M1.2	11303	N13E52	5	22±15	0.45±0.32	4.1%
86	2011-09-24	23:45	23:58	00:09	1440	M1.0	11303	S28W66	8	23± 2	0.43±0.16	2.2%
87	2011-09-25	02:27	02:33	02:37	600	M4.4	11302	N22W87	8	41±12	0.99±0.00	2.4%
88	2011-09-25	04:31	04:50	05:05	2040	M7.4	11302	N13E50	30	90± 4	0.58±0.08	2.4%
89	2011-09-25	08:46	08:49	08:52	360	M3.1	11302	N13E45	11	45± 6	0.63±0.02	1.7%
90	2011-09-25	09:25	09:35	09:53	1680	M1.5	11303	S28W71	10	29± 0	0.86±0.20	4.1%
91	2011-09-25	15:26	15:33	15:38	720	M3.7	11302	N13E44	25	72± 9	0.19±0.02	1.6%
92	2011-09-25	16:51	16:58	17:09	1080	M2.2	11303	N12E41	11	39± 2	0.51±0.06	2.7%
93	2011-09-26	05:06	05:08	05:13	420	M4.0	11302	N12E34	17	64±13	0.43±0.02	2.9%
94	2011-09-26	14:37	14:46	15:02	1500	M2.6	11302	N12E30	28	76± 5	0.28±0.00	1.1%

Table 1—Continued

Nr	Observation date	Start time	Peak time	End time	Duration T(s)	GOES class	NOAA AR	Heliogr. position	Length L(Mm)	Diff. coeff. κ	Diff. index β	Fit q_{fit}
95	2011-09-28	13:24	13:28	13:30	360	M1.2	11302	N11E00	16	51± 5	0.25±0.02	2.6%
96	2011-09-30	18:55	19:06	19:15	1200	M1.0	11305	N09E03	18	64± 7	0.67±0.11	2.6%
97	2011-10-01	08:56	09:59	10:17	4860	M1.2	11305	N09W04	24	68± 6	0.84±0.44	2.2%
98	2011-10-02	00:37	00:50	00:59	1320	M3.9	11305	N10W13	18	59± 8	0.45±0.05	1.6%
99	2011-10-02	17:19	17:23	17:26	420	M1.3	11302	N10W55	12	41± 3	0.27±0.00	2.2%
100	2011-10-20	03:10	03:25	03:44	2040	M1.6	11318	N18W88	11	28± 6	0.27±0.14	3.4%
101	2011-10-21	12:53	13:00	13:08	900	M1.3	11319	N05W79	12	49± 0	0.60±0.13	2.5%
102	2011-10-22	10:00	11:10	13:09	11340	M1.3	11314	N27W87	50	112±23	0.23±0.02	1.7%
103	2011-10-31	14:55	15:08	15:27	1920	M1.1	11313	N20E88	8	28±10	0.45±0.29	3.0%
104	2011-10-31	17:21	18:08	18:50	5340	M1.4	11313	N21E88	8	20± 6	0.49±0.29	1.3%
105	2011-11-02	21:52	22:01	22:19	1620	M4.3	11339	N20E77	16	49± 9	0.43±0.14	3.3%
106	2011-11-03	10:58	11:11	11:20	1320	M2.5	11339	N20E70	12	34± 1	0.30±0.02	1.3%
107	2011-11-03	20:16	20:27	20:32	960	X1.9	11339	N21E64	20	63± 9	0.34±0.05	2.2%
108	2011-11-03	23:28	23:36	23:44	960	M2.1	11339	N20E62	12	45± 2	0.67±0.10	2.1%
109	2011-11-04	20:31	20:40	20:46	900	M1.0	11339	N19E47	12	57±16	0.98±0.42	2.1%
110	2011-11-05	03:08	03:35	03:58	3000	M3.7	11339	N20E47	29	86± 8	0.48±0.13	1.7%
111	2011-11-05	11:10	11:21	11:42	1920	M1.1	11339	N19E41	15	47±10	0.87±0.16	2.1%
112	2011-11-05	20:31	20:38	20:54	1380	M1.8	11339	N21E37	15	42± 3	0.34±0.01	2.4%
113	2011-11-06	00:46	01:03	01:24	2280	M1.2	11339	N20E34	14	38± 4	0.34±0.07	1.7%
114	2011-11-06	06:14	06:35	06:41	1620	M1.4	11339	N21E33	19	52±10	0.19±0.03	3.7%
115	2011-11-09	13:04	13:35	14:12	4080	M1.1	11342	N24E35	39	91±19	0.55±0.04	2.2%
116	2011-11-15	09:03	09:12	09:23	1200	M1.2	11348	N21W72	10	35±10	0.52±0.18	2.7%
117	2011-11-15	12:30	12:43	12:50	1200	M1.9	11346	S19E32	15	41± 7	0.21±0.04	2.6%
118	2011-11-15	22:27	22:35	22:42	900	M1.1	11348	N18W81	9	22± 2	0.04±0.01	1.4%
119	2011-12-25	18:11	18:16	18:20	540	M4.0	11387	S22W26	17	60±14	0.42±0.06	3.2%
120	2011-12-26	02:13	02:27	02:36	1380	M1.5	11387	S21W33	13	56± 6	1.00±0.06	2.2%
121	2011-12-26	20:12	20:30	20:36	1440	M2.3	11387	S21W44	11	41±11	0.65±0.14	2.1%
122	2011-12-29	13:40	13:50	14:01	1260	M1.9	11389	S25E70	11	33± 4	0.43±0.05	3.0%
123	2011-12-29	21:43	21:51	21:59	960	M2.0	11389	S25E67	14	59± 0	0.98±0.14	1.6%
124	2011-12-30	03:03	03:09	03:13	600	M1.2	11389	S25E67	9	27± 2	0.30±0.13	4.0%
125	2011-12-31	13:09	13:15	13:19	600	M2.4	11389	S25E46	13	38± 6	0.25±0.06	3.6%
126	2011-12-31	16:16	16:26	16:34	1080	M1.5	11389	S25E42	15	51± 3	0.58±0.08	2.9%
127	2012-01-14	13:14	13:18	13:20	360	M1.4	11401	N14E88	8	21± 5	0.10±0.08	3.0%
128	2012-01-17	04:41	04:53	05:07	1560	M1.0	11401	N18E53	13	38± 2	0.52±0.02	1.5%
129	2012-01-18	19:04	19:12	19:27	1380	M1.7	11401	N17E32	16	59±11	0.17±0.04	2.5%
130	2012-01-19	13:44	16:05	17:50	14760	M3.2	11402	N32E27	38	76±11	0.45±0.10	1.9%
131	2012-01-23	03:38	03:59	04:34	3360	M8.7	11402	N33W21	37	111± 9	0.98±0.09	1.2%
132	2012-01-27	17:37	18:37	18:56	4740	X1.7	11402	N33W85	40	114± 8	0.95±0.07	1.7%
133	2012-02-06	19:31	20:00	20:17	2760	M1.0	11410	N19W62	28	89± 5	0.54±0.14	1.6%
134	2012-03-02	17:29	17:46	18:07	2280	M3.3	11429	N19W62	10	36± 1	0.75±0.03	1.6%
135	2012-03-04	10:29	10:52	12:16	6420	M2.0	11429	N16E65	23	48± 2	0.48±0.03	1.7%
136	2012-03-05	02:30	04:09	04:43	7980	X1.1	11429	N19E58	32	74± 5	0.44±0.03	1.7%
137	2012-03-05	19:10	19:16	19:21	660	M2.1	11429	N16E45	10	32± 2	0.36±0.03	2.3%
138	2012-03-05	19:27	19:30	19:32	300	M1.8	11429	N16E45	7	26± 5	0.34±0.18	3.0%
139	2012-03-05	22:26	22:34	22:42	960	M1.3	11429	N16E43	9	33± 3	0.46±0.01	2.3%
140	2012-03-06	00:22	00:28	00:31	540	M1.3	11429	N16E42	8	27± 5	0.38±0.20	3.1%
141	2012-03-06	01:36	01:44	01:50	840	M1.2	11429	N16E41	8	28± 3	0.40±0.04	2.3%

Table 1—Continued

Nr	Observation date	Start time	Peak time	End time	Duration T(s)	GOES class	NOAA AR	Heliogr. position	Length L(Mm)	Diff. coeff. κ	Diff. index β	Fit q_{fit}
142	2012-03-06	04:01	04:05	04:08	420	M1.0	11429	N16E39	9	47± 6	0.96±0.09	2.0%
143	2012-03-06	07:52	07:55	08:00	480	M1.0	11429	N17E40	8	41± 2	0.87±0.05	2.5%
144	2012-03-06	12:23	12:41	12:54	1860	M2.1	11429	N21E40	15	55±10	1.07±0.16	1.3%
145	2012-03-06	21:04	21:11	21:14	600	M1.3	11429	N16E30	10	38± 9	0.59±0.11	2.0%
146	2012-03-06	22:49	22:53	23:11	1320	M1.0	11429	N19E32	11	35± 8	0.62±0.07	1.8%
147	2012-03-07	00:02	00:24	00:40	2280	X5.4	11429	N18E31	37	100±12	0.60±0.01	1.9%
148	2012-03-07	01:05	01:14	01:23	1080	X1.3	11430	N15E26	35	105± 6	0.63±0.03	0.8%
149	2012-03-09	03:22	03:53	04:18	3360	M6.3	11429	N15W03	33	82± 5	0.50±0.01	3.6%
150	2012-03-10	17:15	17:44	18:30	4500	M8.4	11429	N17W24	30	77± 5	0.40±0.01	1.2%
151	2012-03-13	17:12	17:41	18:25	4380	M7.9	11429	N17W66	36	83± 6	0.73±0.01	1.3%
152	2012-03-14	15:08	15:21	15:36	1680	M2.8	11432	N13E05	18	63± 6	0.55±0.03	2.0%
153	2012-03-15	07:23	07:52	08:08	2700	M1.8	11432	N14W03	21	66± 6	0.61±0.03	1.3%
154	2012-03-17	20:32	20:39	20:42	600	M1.3	11434	S20W25	10	42± 4	0.51±0.02	1.1%
155	2012-03-23	19:34	19:40	19:44	600	M1.0	11445	S20W25	7	23± 2	0.25±0.01	2.5%

Table 2. Statistical results of observables and model parameters of 155 analyzed flare events during 2010/05/13-2011/03/31.

Parameter	Range	Mean	Median	Powerlaw slope
Flare duration (GOES rise time) $T(s) =$	120-8460	1030 ± 1050	660	2.17
AIA 335 time interval $T_{AIA}(s) =$	336-10992	1806 ± 1579	1296	
Length (flare radius) $L(Mm) =$	5.5 – 51	19 ± 10	16	1.96
Peak flux GOES $F_{GOES}(W m^{-2}) =$	$(1 - 69) \times 10^{-5}$	$(4.1 \pm 7.8) \times 10^{-5}$	7.8×10^{-5}	1.92
Total flux AIA 335 Å $F_{AIA}(DN/s) =$	$(7.2 - 2462) \times 10^4$	$(4.4 \pm 4.7) \times 10^6$	2.5×10^6	1.34
Mean velocity $v(km/s) =$	3-103	15 ± 12	11	2.72
Maximum velocity $v_{max}(km/s) =$	8-550	80 ± 85	57	1.83
Diffusion coefficient $\kappa(km s^{-\beta/2}) =$	19-139	56 ± 24	52	
Diffusion index $\beta =$	0.04-1.35	0.53 ± 0.27	0.49	
Goodness-of-fit $q_{fit} = \Delta r/r_{max}(\%) =$	0.8-4.2	2.2 ± 0.7	2.1	

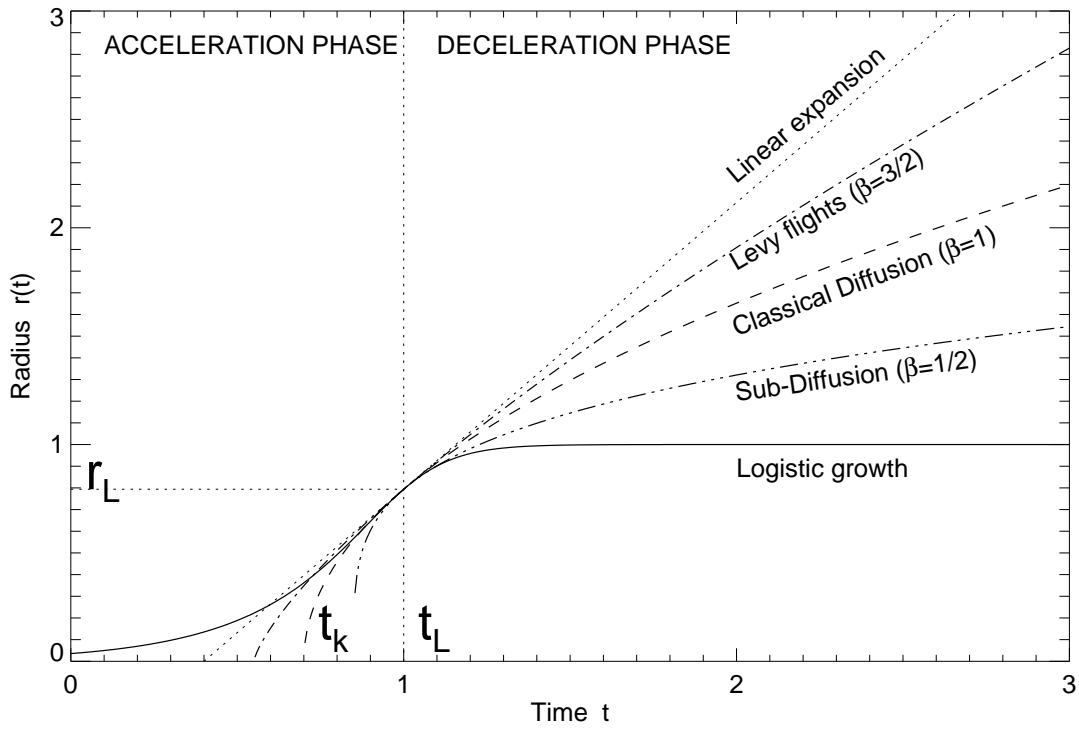


Fig. 1.— Comparison of spatio-temporal evolution models: Logistic growth with parameters $t_L = 1.0$, $r_\infty = 1.0$, $\tau_G = 0.1$, sub-diffusion ($\beta = 1/2$), classical diffusion ($\beta = 1$), Lévy flights or super-diffusion ($\beta = 3/2$), and linear expansion ($r \propto t$). All three curves intersect at $t = t_L$ and have the same speed $v = (dr/dt)$ at the intersection point at time $t = t_L$.

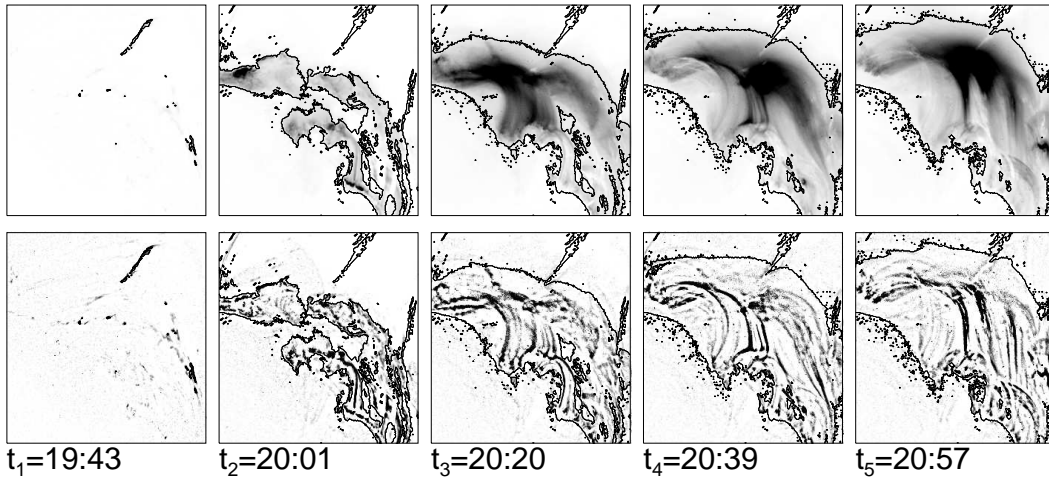
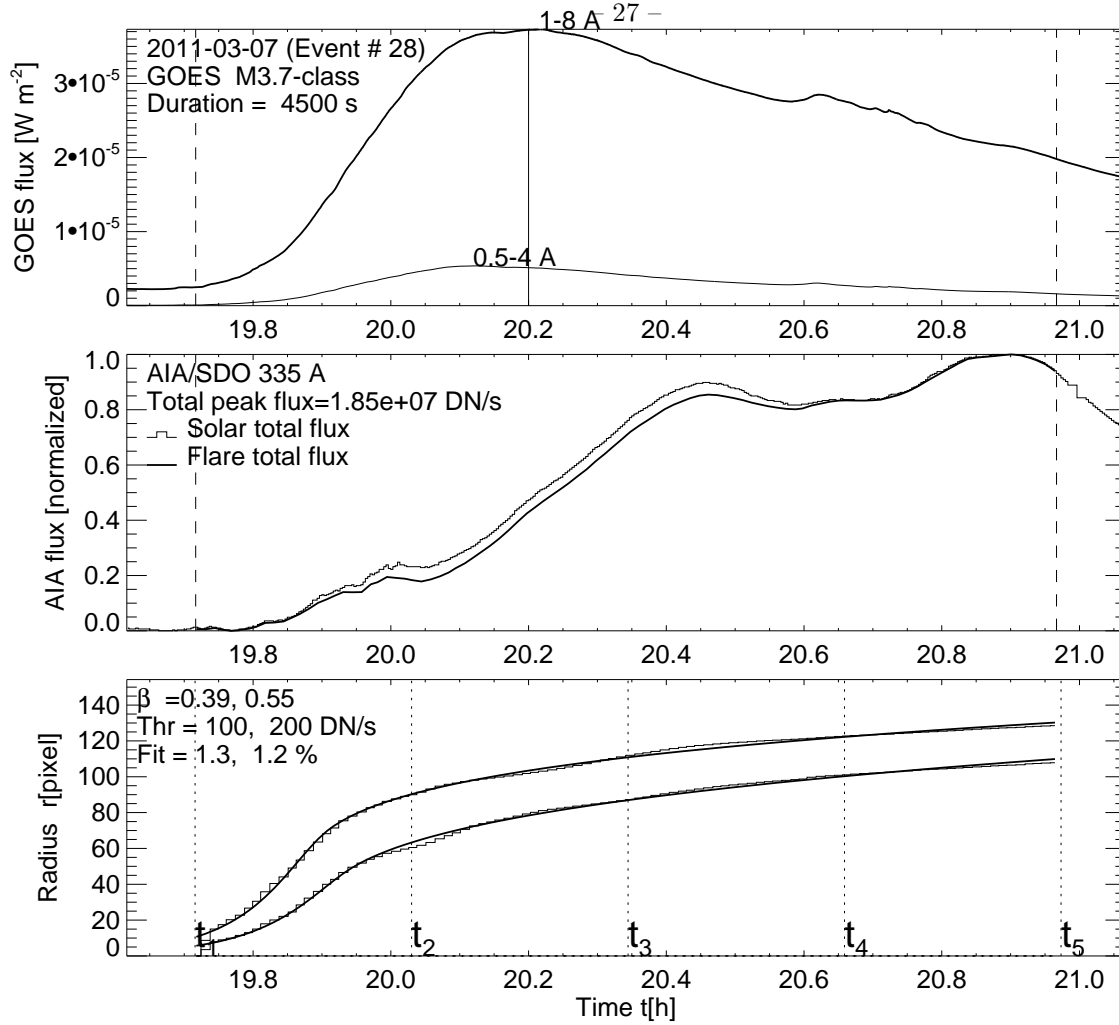


Fig. 2.— The flare event #28 was observed on 2011 Mar 7, 19:43–20:58 UT, with AIA/SDO 335 Å, with GOES time profiles (top panel), the total flux (second panel), the spatio-temporal evolution of the radius $r(t) = \sqrt{A(t)/\pi}$ of the time-integrated flare area $A(t)$ for two thresholds, $F_{thresh} = 100, 200$ DN/s (third panel; histogrammed), fitted with the anomalous diffusion model (third panel; solid curve), and 5 snapshots of the baseline-subtracted flux (fourth row) and highpass-filtered flux (bottom row), with the threshold flux $F_{thresh} = 100$ DN/s shown as contour.

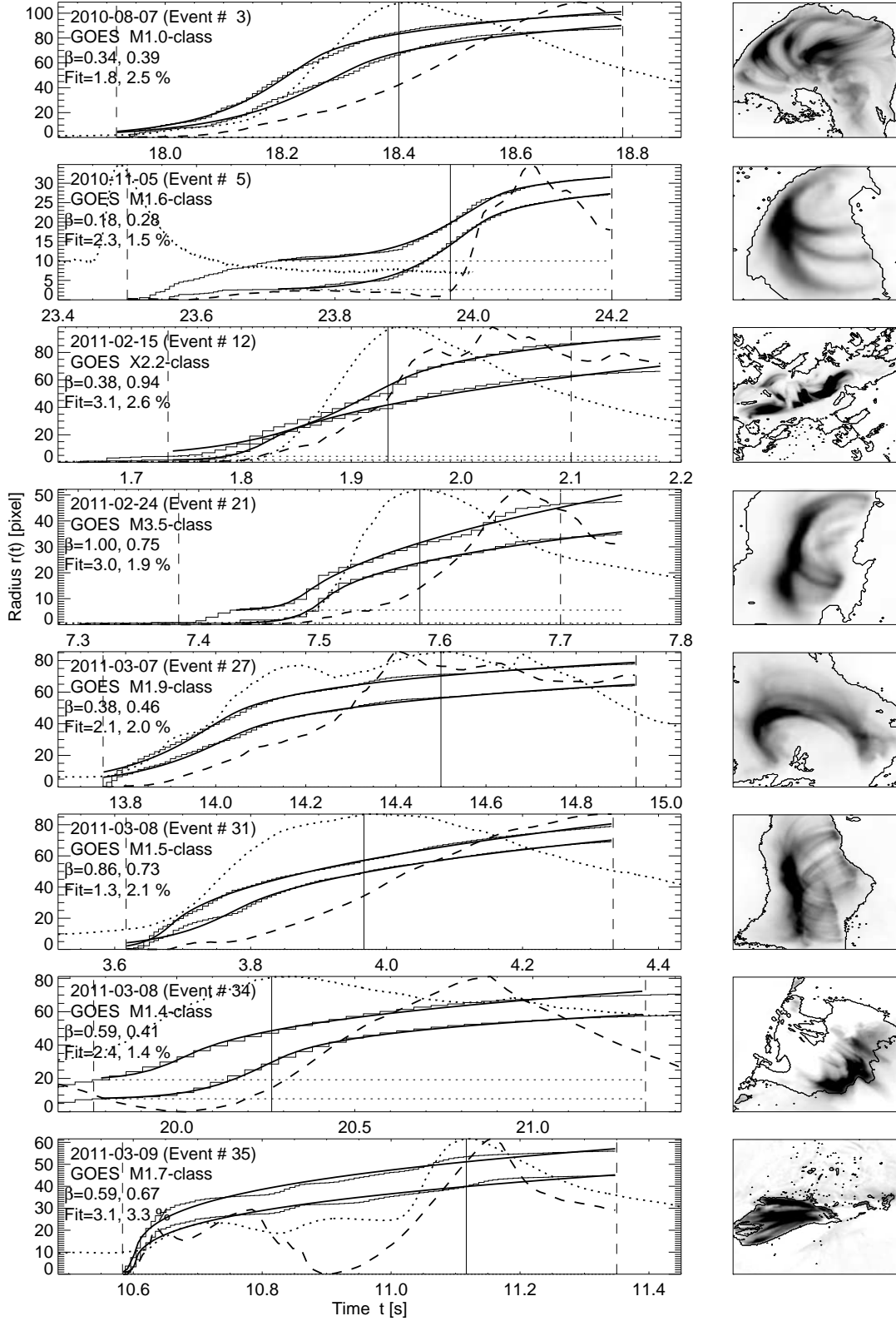
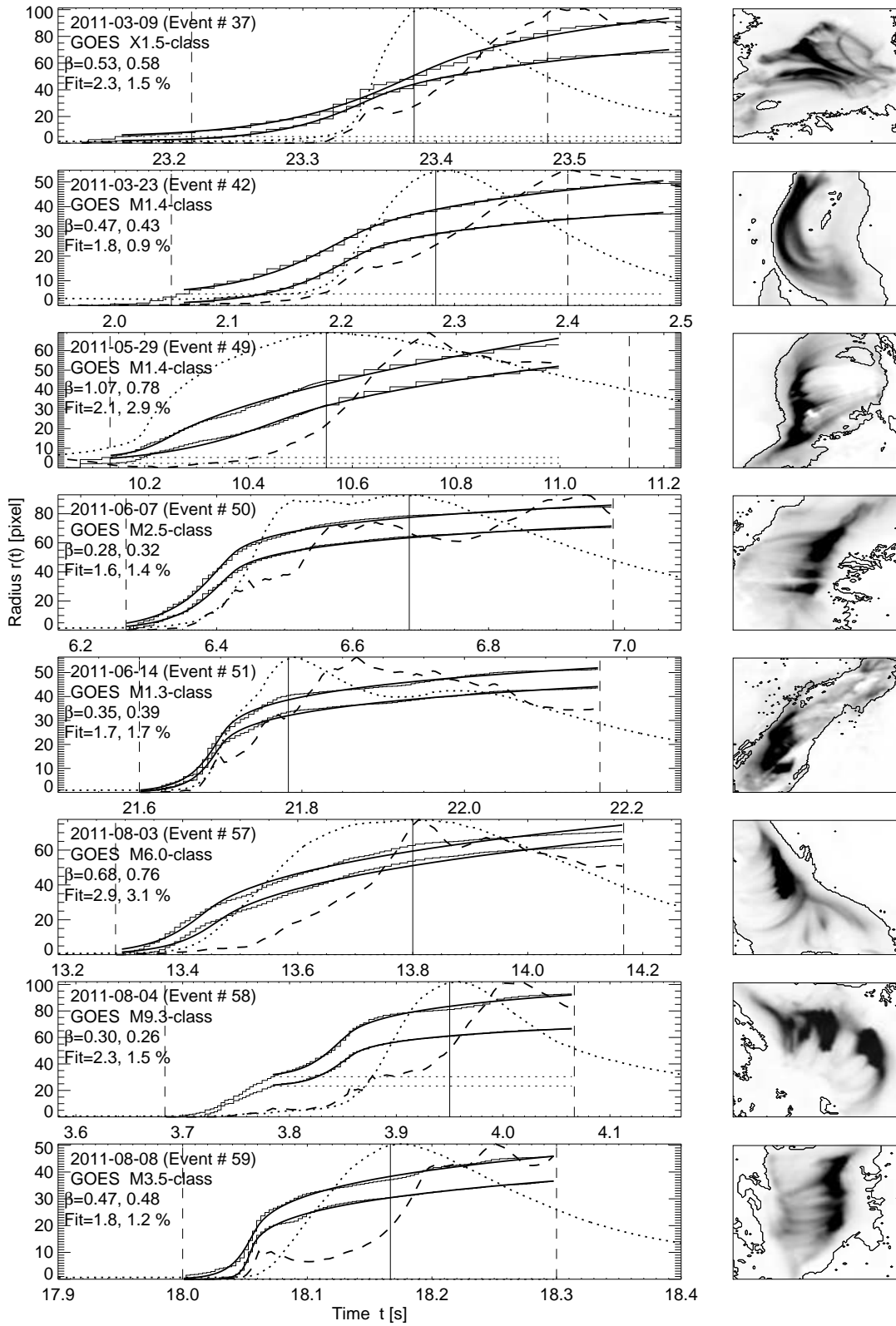
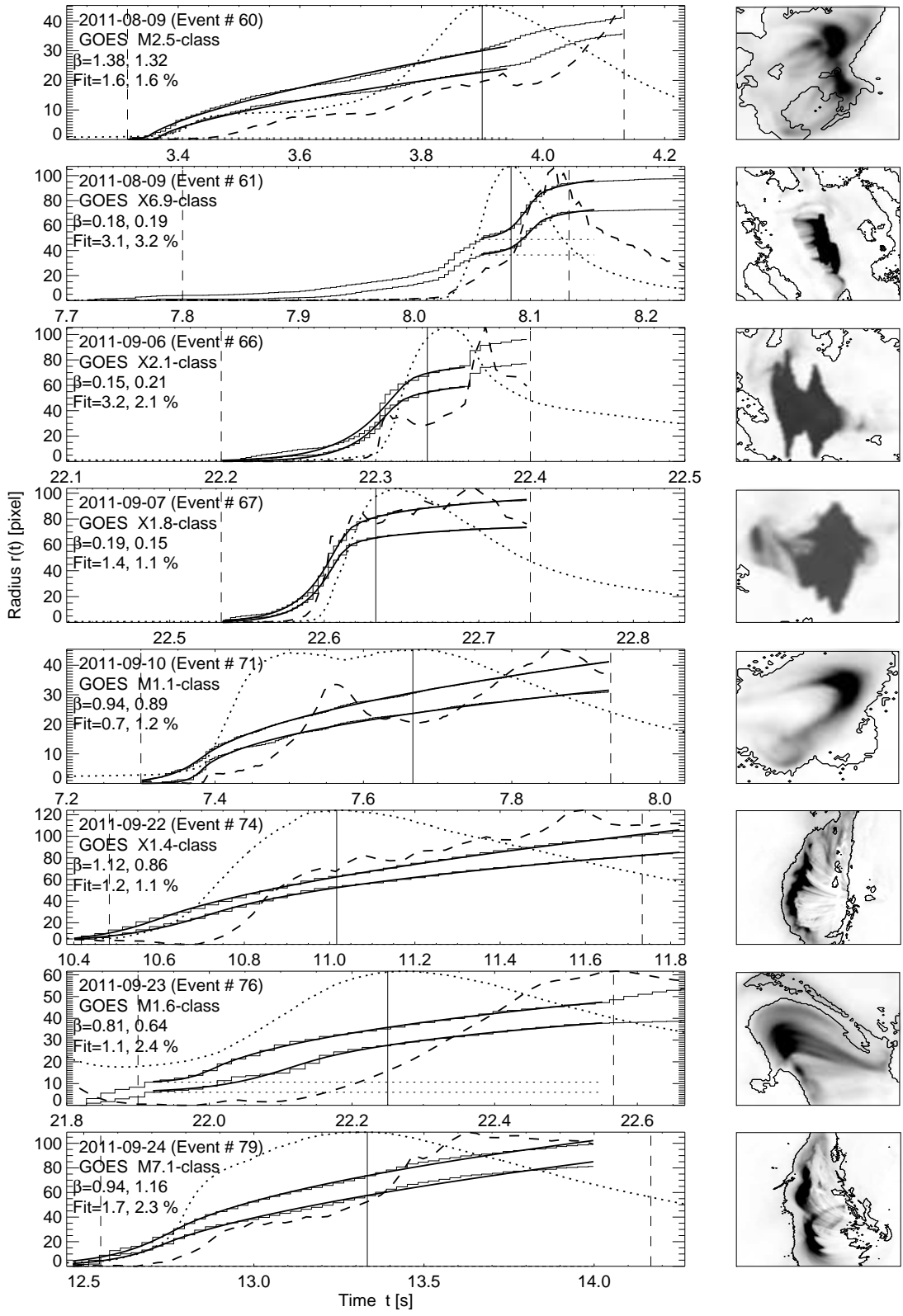
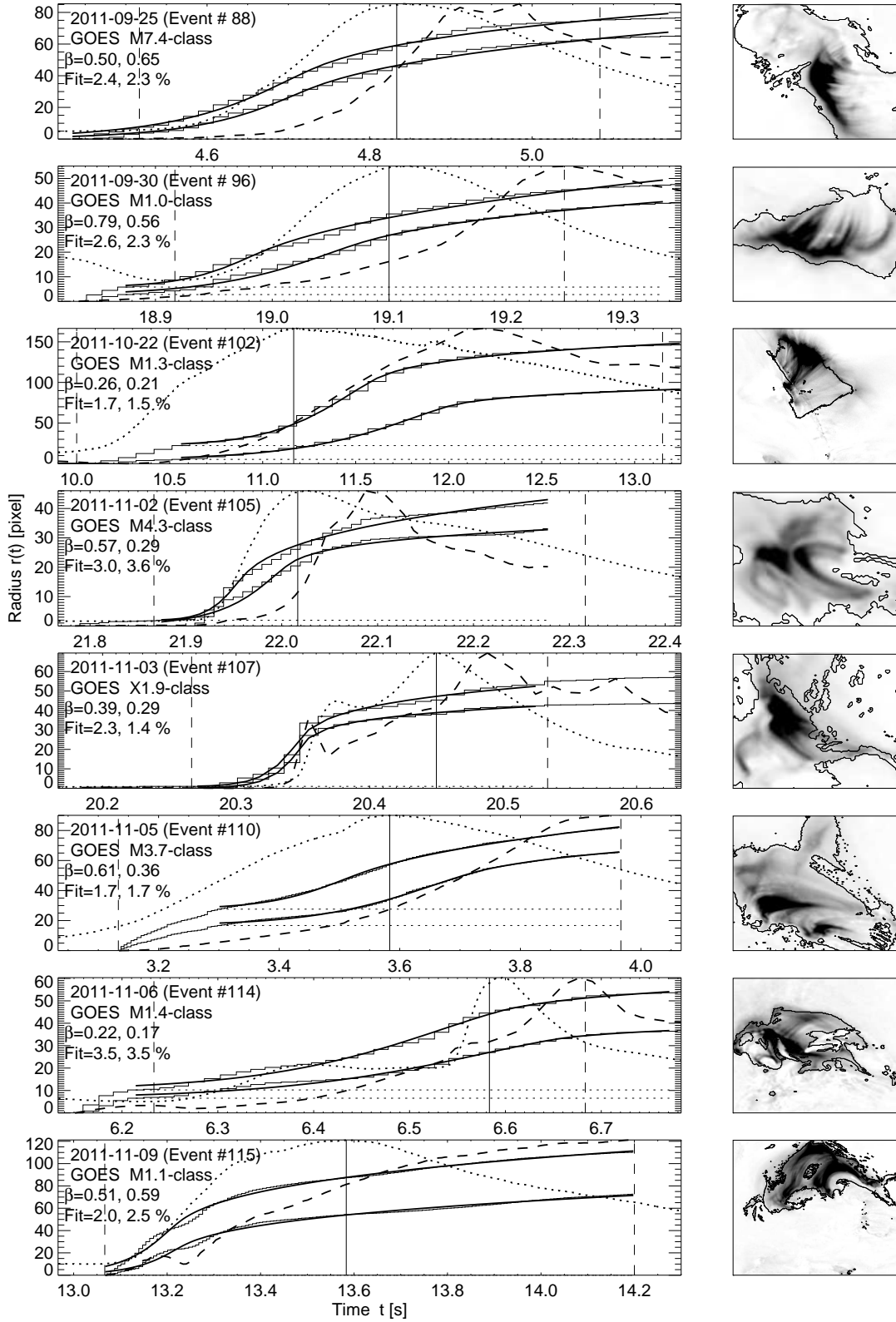
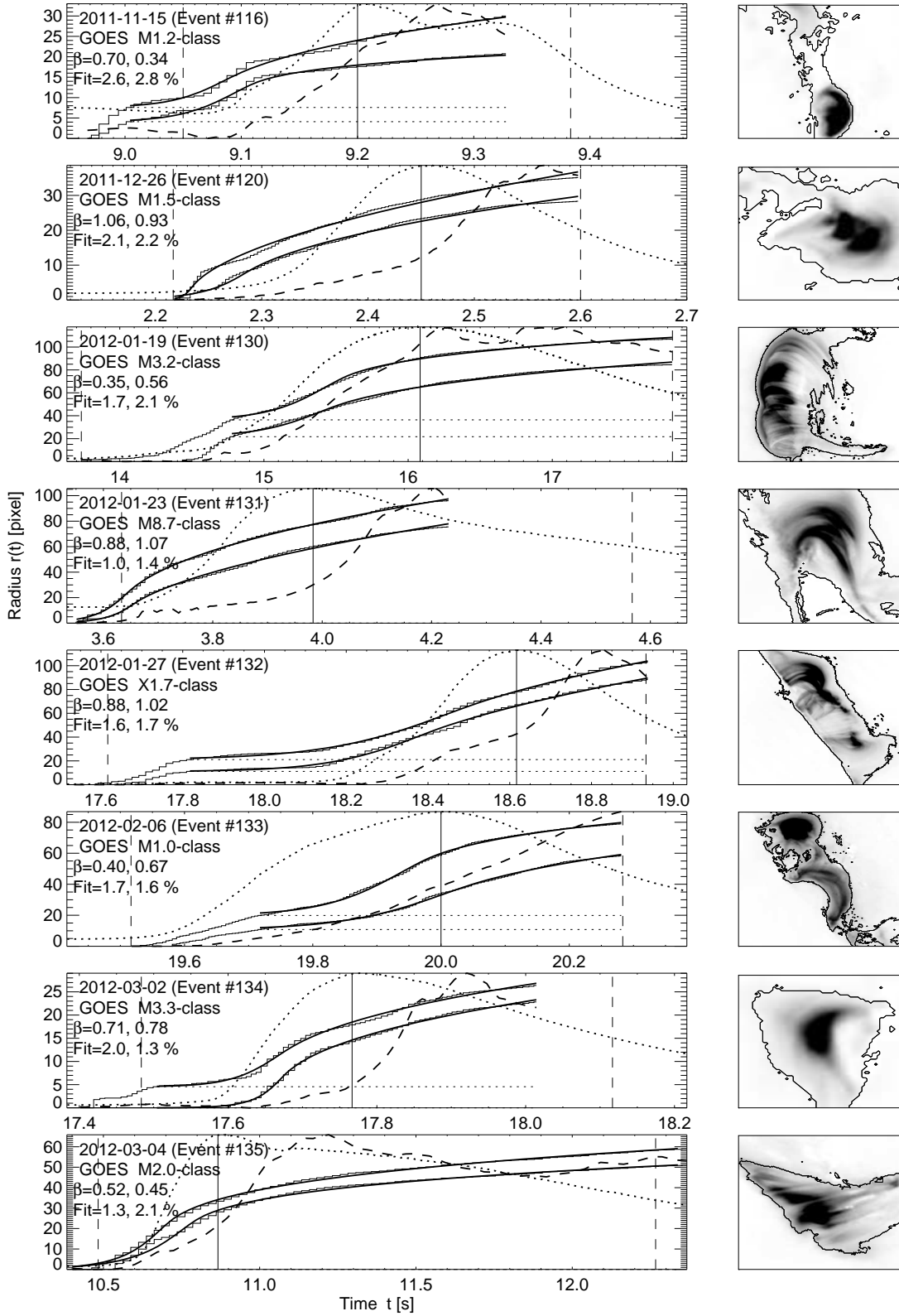


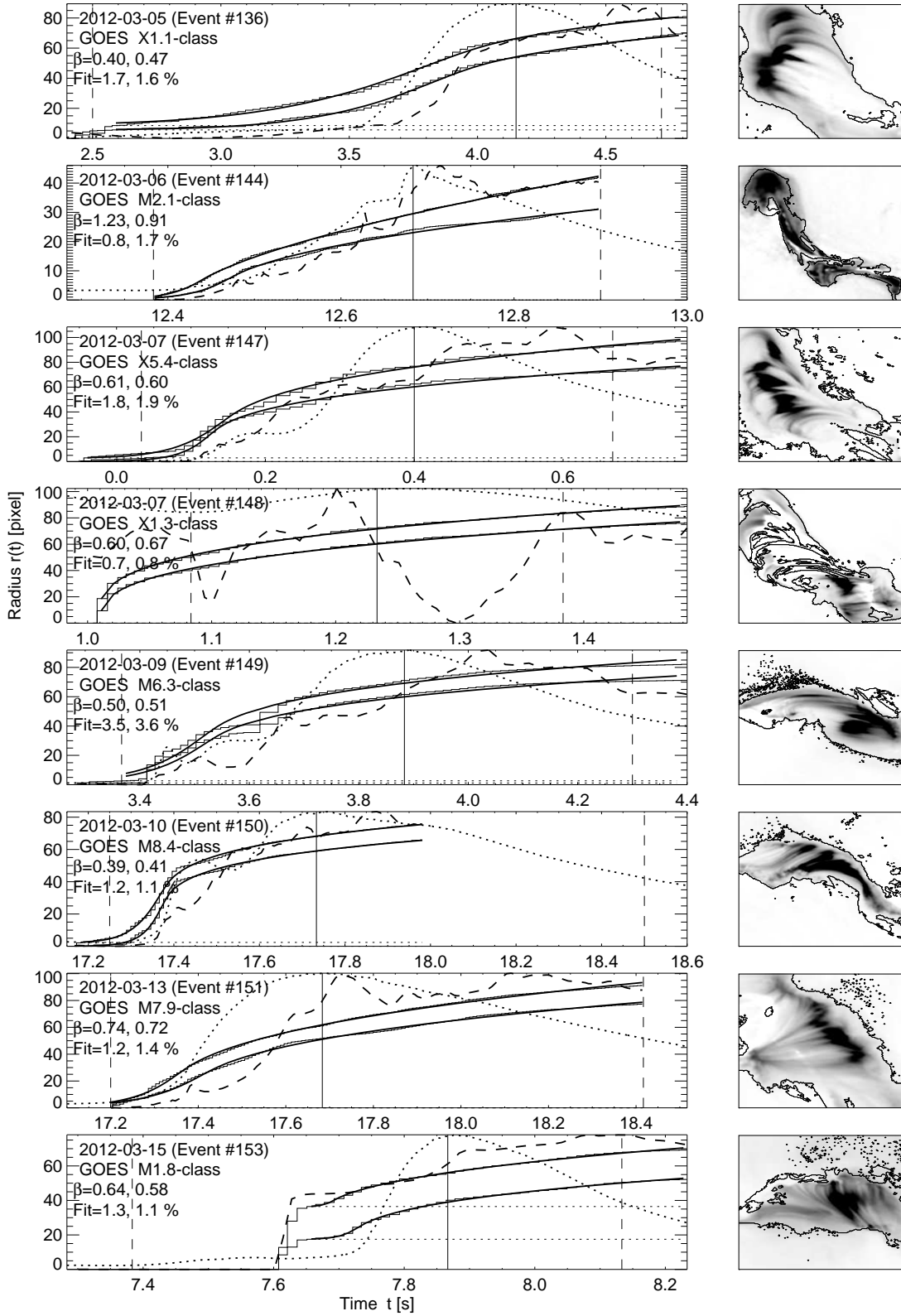
Fig. 3.— A selection of analyzed flare events, showing the GOES 1-8 Å time profile (dotted curve), the AIA 335 Å total flux (dashed curve), the measured radius of the flare area for two flux thresholds (histograms), the best-fit diffusion model (solid curve), and preflare-subtracted AIA 335 Å image at the end of the flare, with the contours of the flux threshold of $F_{thresh} = 100$ DN/s indicated (right panels).











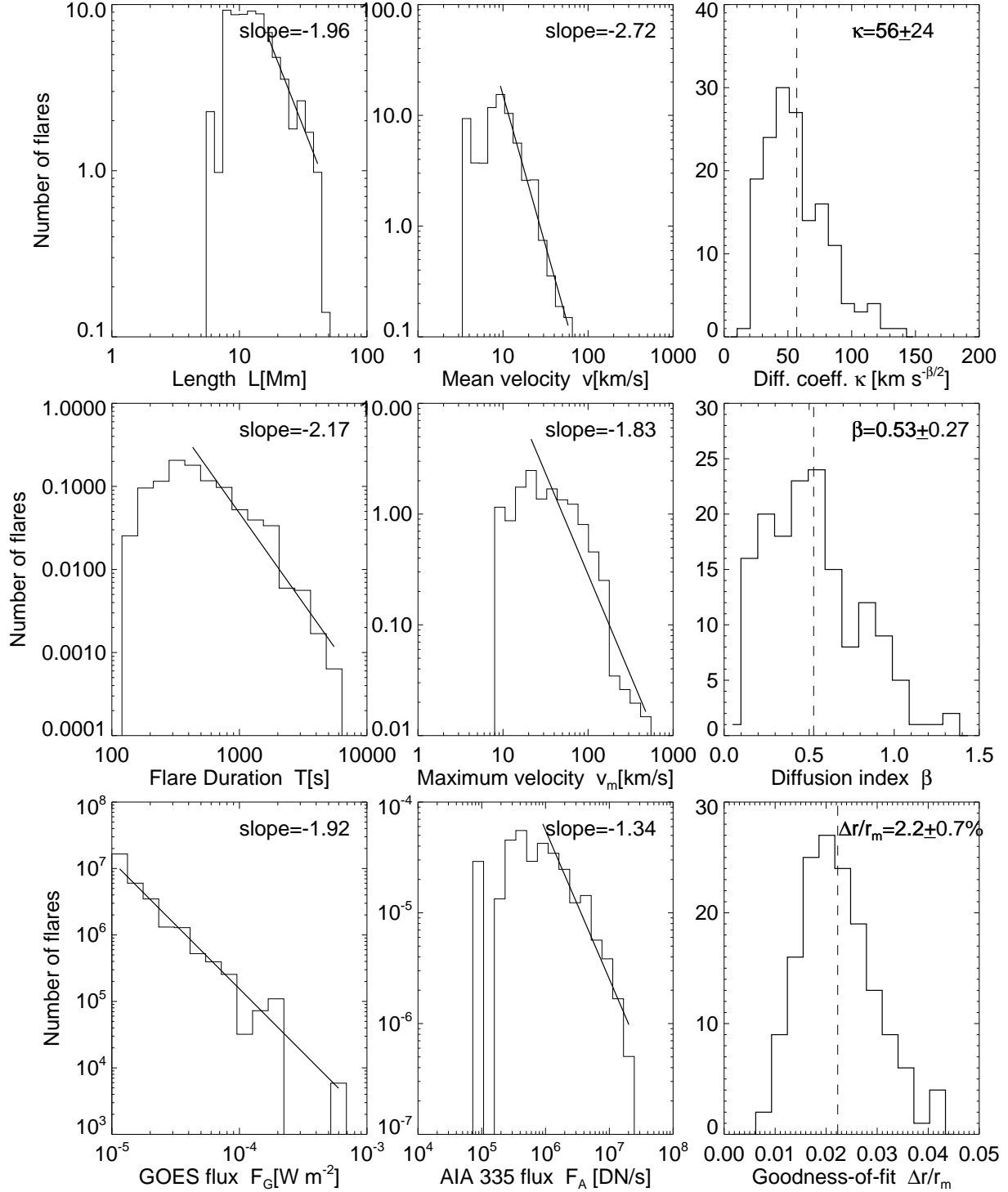


Fig. 4.— Distributions of various observed parameters (L, T, F_G, v, v_m, F_A) in log-log format with powerlaw fit (left and middle column), and best-fit model parameters ($\kappa, \beta, \Delta r/r_m$) with linear histogram and mean and standard deviation indicated (right column).

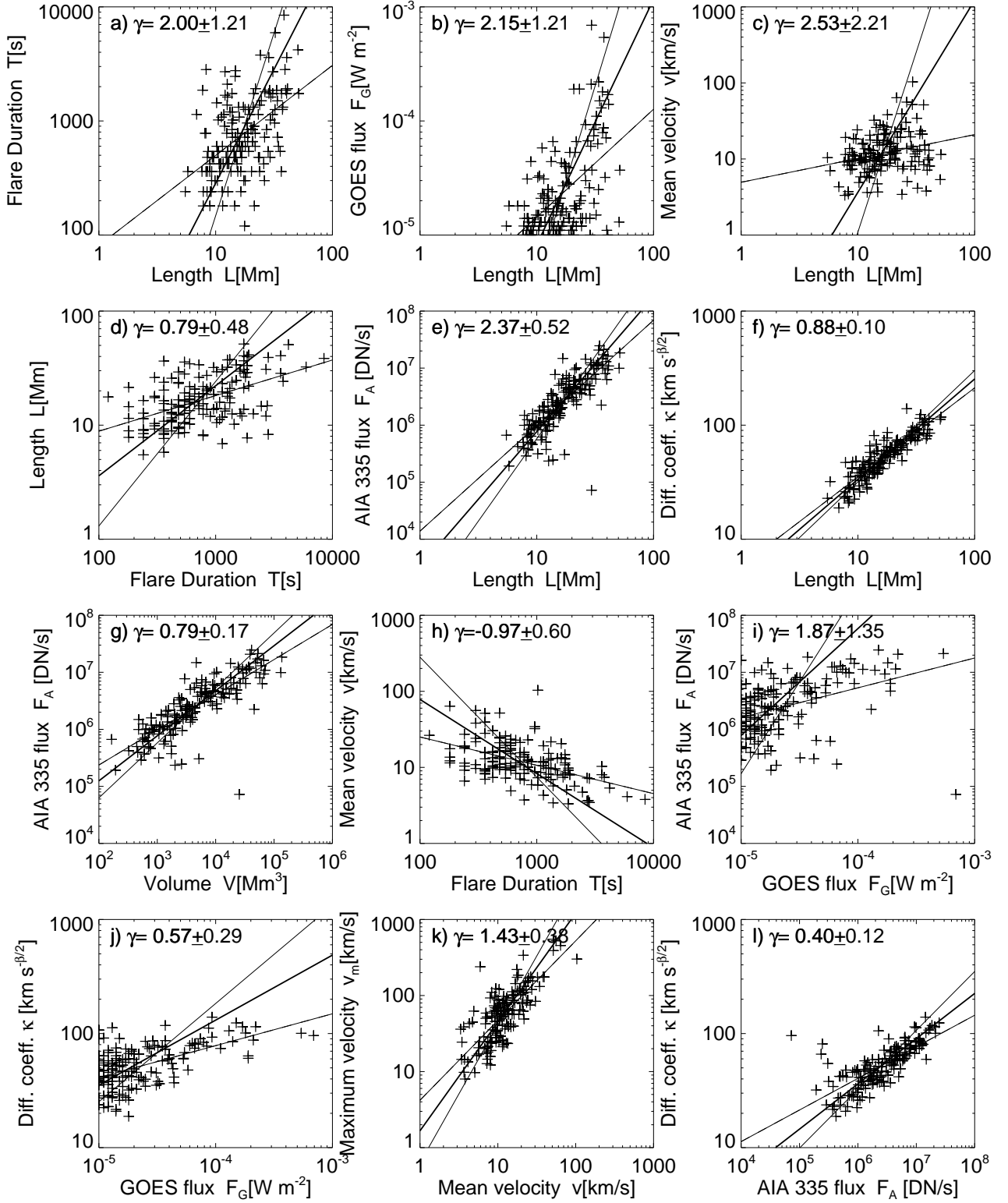


Fig. 5.— Correlations between observed and best-fit parameters. The linear regression fits are shown for $y(x)$ and $x(y)$ (thin lines), and for the arithmetic mean (thick lines).